The Astrophysical Journal, 799:13 (18pp), 2015 January 20 doi:10.1088/0004-637X/799/1/13

STRONG C^+ EMISSION IN GALAXIES AT $z \sim 1$–2: EVIDENCE FOR COLD FLOW ACCRETION POWERED STAR FORMATION IN THE EARLY UNIVERSE

Drew Brisbin[1,2], Carl Ferkinhoff[2,3], Thomas Nikola[2], Stephen Parshley[2], Gordon J. Stacey[4], Henrik Spoon[2], Steven Hailey-Dunsheath[5], and Aprajita Verma[6]
[1] National Radio Astronomy Observatory, Charlottesville, VA 22903, USA; dbrisbin@nrao.edu
[2] Center for Radiophysics & Space Research, Cornell University, Ithaca, NY 14853, USA
[3] Max-Planck-Institut für Astronomie, Konigstuhl 17, D-69117 Heidelberg, Germany
[4] Department of Astronomy, Cornell University, Ithaca, NY 14853, USA
[5] California Institute of Technology, Mail Code 301-17, 1200 East California Boulevard, Pasadena, CA 91125, USA
[6] University of Oxford, Oxford Astrophysics, Denys Wilkinson Building, Keble Road, Oxford, OX1 3RH, UK
Received 2013 November 16; accepted 2014 November 3; published 2015 January 12

ABSTRACT

We have recently detected the [C II] 157.7 μm line in eight star-forming galaxies at redshifts 1 to 2 using the redshift (z) Early Universe Spectrometer (ZEUS). Our sample targets star formation dominant sources detected in PAH emission. This represents a significant addition to [C II] observations during the epoch of peak star formation. We have augmented this survey with observations of the [O I] 63 μm line and far infrared photometry from the PACS and SPIRE *Herschel* instruments as well as *Spitzer* IRS spectra from the literature showing PAH features. Our sources exhibit above average gas heating efficiency, many with both [O I]/FIR and [C II]/FIR of $\sim$1% or more. The relatively strong [C II] emission is consistent with our sources being dominated by star formation powered photo-dissociation regions, extending to kiloparsec scales. We suggest that the star formation mode in these systems follows a Schmidt–Kennicutt law similar to local systems, but at a much higher rate due to molecular gas surface densities 10–100 times that of local star-forming systems. The source of the high molecular gas surface densities may be the infall of neutral gas from the cosmic web. In addition to the high [C II]/FIR values, we also find high [C II]/PAH ratios and, in at least one source, a cool dust temperature. This source, SWIRE 4–5, bears a resemblance in these diagnostics to shocked regions of Stephan's Quintet, suggesting that another mode of [C II] excitation in addition to normal photoelectric heating may be contributing to the observed [C II] line.

Key words: galaxies: evolution – galaxies: high-redshift – galaxies: ISM – galaxies: star formation – photon-dominated region (PDR) – submillimeter: galaxies

1. INTRODUCTION

With recent developments in submillimeter spectroscopy, including the conclusion of extensive observations with the *Herschel Space Observatory*[7] (Pilbratt et al. 2010), ALMA beginning full science operations, and ongoing developments with other ground-based interferometers and large single disk telescopes, the study of the redshifted universe in the far-infrared (FIR) has come into its prime.

Emission from ionized carbon is one important tool for FIR studies of early galaxies. Carbon is the fourth most abundant element in the universe, and it takes 11.3 eV photons to form C+, so the low-lying (91 K above ground) 157.7 μm [C II] fine-structure line was long ago predicted to be the dominant coolant of the neutral ISM (Dalgarno & McCray 1972). The [C II] line is also usually optically thin and suffers very little extinction; thus, it is an excellent probe of the properties of the atomic gas heated by the far-UV (FUV; 6–13.6 eV) flux in galaxies. Indeed, the first [C II] detections from local galaxies revealed that the [C II] line can be the brightest single emission line from star-forming galaxies, amounting to between 0.1% and 1% of the total FIR luminosity[8] (Crawford et al. 1985; Stacey et al. 1991).

The [C II] line luminosity is closely correlated with CO emission. Thus, while some [C II] does arise in ionized gas, a picture has emerged where most ($\sim$70%) arises from the warm, dense, neutral gas of photo-dissociation regions (PDRs; Stacey et al. 1991; Oberst et al. 2006; Vasta et al. 2010). The PDR heating is dominated by FUV radiation from nearby early-type stars. Nearly all of the UV intercepted by dust is absorbed and converted to long wavelength thermal emission, giving rise to the FIR continuum. A small fraction ($\sim$1%) of the UV photons eject hot electrons from dust and PAH grains, heating the gas which, in turn, collisionally excites the [C II] line (Tielens & Hollenbach 1985).

For moderate gas densities ($n < 10^4$ cm^{-3}) and FUV field strengths ($G_0 < 10^3$)[9] that are typical in star-forming galaxies averaged over large scales, the [C II] line is the primary coolant for gas in PDRs. The ratio of power in this line to the FIR continuum represents the gas heating as a fraction of the total UV power. It is a first measure of the "gas heating efficiency." A more complete measure includes the [O I] 63 μm line, which, due to its higher critical density for thermalization ($n_{\rm crit} \sim 4.7\times10^5$ cm^{-3}, versus 2.8×10^3 cm^{-3} for [C II]) and greater energy above ground for the emitting level (228 K), becomes the dominant PDR coolant at higher densities and FUV field intensities (e.g., Pound & Wolfire 2008; Kaufman et al. 2006). Together, the two fine structure lines constrain n and G_0 for PDRs. However, since the gas densities for most galaxies are between 10^3 and

[7] *Herschel* is an ESA space observatory with science instruments provided by the European-led Principal Investigator consortia and with important participation from NASA.
[8] In this paper, FIR refers to 42.5–122.5 μm. This is one of the most common conventions in the literature. To compare to other samples and models, we will also make use of several other conventional wavelength ranges including 30–1000 μm, 40–500 μm, and 8–1000 μm where explicitly noted.
[9] G_0, the Habing flux, parameterizes the far-UV flux in terms of a typical ISM FUV flux, $G_0 = F_{\rm FUV}/1.6\times10^{-6}$ W m^{-2}.

10^5 cm^{-3}, the [C II]/FIR ratio is in and of itself a good tracer of the heating efficiency (Stacey et al. 2010b). In PDR models with moderate densities, [C II]/FIR is inversely proportional to G_0. ISO-based studies showed that [C II]/FIR tends to be an order of magnitude smaller in local ultra luminous infrared galaxies (ULIRGs; $L_{\rm FIR} > 10^{12} L_\odot$) relative to normal star-forming galaxies—a characteristic sometimes referred to as the "[C II] deficit" (Luhman et al. 2003). This relationship shows that, in the local universe, ULIRGs are not simply scaled up normal galaxies. Something is fundamentally different about their star formation to cause this deficient [C II] emission.

Stacey et al. (2010b) demonstrated that the [C II] deficit does not hold throughout the universe. The observed [C II] deficit in the local universe is only indicative of the underlying star formation conditions in local ULIRGs. PDR models demonstrate that low [C II]/FIR on a galactic scale indicates very intense UV fields ($G \gtrsim 10^4$) in star-forming media. In local galaxies, the star bursting episodes that give rise to such intense UV fields generally occur in ULIRGs. Recent major mergers leading to localized and very intense star formation are sources of extreme luminosity in these local systems. During the epoch of peak star formation, ULIRGs make up a larger fraction of the total star formation activity, and thus we might expect a continuation of the locally observed [C II] deficit. Stacey et al. (2010b) showed, however, that at $z = 1$–2 systems with extreme (ULIRG and HyLIRG) luminosities do not necessarily have suppressed [C II]/FIR ratios or extreme UV fields. Stacey et al. (2010b) instead finds that the high-luminosity, star-formation-dominated systems in this epoch have very extended star formation regions with more moderate FUV fields. This is consistent with complementary lines of evidence supporting extended star formation (Pope et al. 2006; Farrah et al. 2008; Menéndez-Delmestre et al. 2009) and has contributed to a paradigm shift in the accepted nature of star formation in the early universe. Rather than being powered solely by major mergers, a significant population of ULIRGs in the early universe are forming stars in a mode similar to normal local galaxies. The observational data could be explained by star formation proceeding through accretion of gas from the intergalactic medium, which builds to surface densities of ∼10–100 times that of the Milky Way. This is often seen in subgalactic star formation regions nearby and is adequately described by the Schmidt–Kennicutt star formation law (Schmidt 1959; Kennicutt 1998). We suggest that in these galaxies at high redshift, similar star formation is occurring on a near galaxy-wide scale, leading to moderate UV field intensities ($G_0 \sim$ 100–1000), but very large luminosities due to their very large size. This is consistent with several recent findings by Tacconi et al. (2010), Daddi et al. (2010), Ivison et al. (2011), Riechers et al. (2011), and Hodge et al. (2012), which all show widespread CO emission ∼several kiloparsec in extent and indicate high molecular gas fractions in normal star-forming galaxies at a similar epoch. Although they are certainly present in the early universe (e.g., Ferkinhoff et al. 2014), major mergers are not required to explain the very large intrinsic luminosities ($L > 10^{12} L_\odot$) in this epoch.

Motivated by the results of our previous work, we have undertaken an expanded [C II] survey of eight $z = 1$–2 sources with the redshift (z) and Early Universe Spectrometer (ZEUS) on CSO; a survey that we have augmented with [O I] 63 μm observations from the *Herschel* PACS instrument (Poglitsch et al. 2010). This survey represents the continuation of the original work by Stacey et al. (2010b), which placed an equal emphasis on sources whose luminosities were active galactic nucleus (AGN) dominant, star formation dominant (SF-D), or of mixed nature. In this follow up survey, we have focused on SF-D systems. We confirm that the [C II] deficit is not a ubiquitous trait in star formation powered ULIRGs in the redshift 1–2 epoch. We also find moderately intense ($G_0 \sim 10^{2-3}$) UV fields distributed over very large (several kiloparsec) scales within galaxies. A similar analysis of [O I] 63 μm in the sources from the original Stacey et al. (2010b) sample will be found in S. Hailey-Dunsheath (in preparation).

The characterization of our sources as SF-D is based on evidence from the literature without consideration of our [C II] observations. It can generally be interpreted as a characterization of the dominant power source for the total infrared (TIR) (8–1000 μm) luminosity. AGN dominant sources have TIR power dominated by the mid-IR (MIR), while SF-D sources have TIR SEDs dominated by the FIR band. Due to the inhomogeneous nature of background data on our varied source set, however, the precise criteria for characterization is not uniform.

In addition to [C II] and [O I], many of our sources have been observed photometrically with PACS or SPIRE (Griffin et al. 2010), either as part of our own OT2 program, the Herschel Multi-tiered Extragalactic Survey (HerMES; Oliver et al. 2012), or *SEDs and energetics of lensed UV-bright high redshift galaxies* (PI: Dieter Lutz, ObsID 13422210503, 1342221289, 1342221290, 1342221291, 1342221292.) We have used these data along with photometry collected from the literature to provide uniformly processed SEDs. In choosing our survey sample, we emphasized luminous sources with PAH emission detected in the MIR with the *Spitzer* Infrared Spectrograph (IRS)[10] spectrometer (Houck et al. 2004). This selection criteria strongly biases our sample toward SF-D systems. We have used these IRS spectra to analyze the presence and nature of PAHs.

The structure of the paper is as follows. In Section 2, we present our observations, including the overall survey methodology. In Section 3, we discuss notes on individual sources. In Section 4, we present our data analysis and results for our global sample and individual sources. In Section 5, we discuss the physical interpretation of our results and their implications for the $z > 1$ universe, and finally, in Section 6, we make concluding remarks.

2. INSTRUMENTATION AND OBSERVATIONS

We conducted [C II] observations using ZEUS at the 10.4 m Caltech Submillimeter Observatory (CSO) on Mauna Kea. ZEUS is well described in the literature (Stacey et al. 2007; Hailey-Dunsheath 2009) so we only briefly describe it here. ZEUS is an echelle grating spectrometer designed to operate over the 350 and 450 μm telluric transmission windows. It has a 1×32 pixel thermistor sensed bolometer detector array that yields a 32 element spectrum split into the 350 and 450 μm bands for a single beam. The detector array and optics are designed to maximize sensitivity to broad lines of widths of ∼a few hundred km s^{-1}—well matched for detecting emission lines from distant galaxies. The resolving power varies by wavelength, but is ∼1000 (velocity resolution ∼300 km s^{-1}), with each pixel sampling one spectral resolution element.

Observations of eight sources took place over three observing runs in 2010 January, 2011 January, and 2011 March. We used

[10] The IRS was a collaborative venture between Cornell University and Ball Aerospace Corporation funded by NASA through the Jet Propulsion Laboratory and the Ames Research Center.

Table 1
ZEUS Observing Log

Source	R.A.	Decl.	$z_{[C\,II]}$	Obs. Dates	t_{los}
MIPS 22530	17h23m03.3s	59d16m00.2s	1.9501	3/15/2011	15.4%
SWIRE3 J104343.93+571322.5 (SWIRE 3-9)	10h43m43.9s	57d13m22.5s	1.7348	3/18/11	23.9%
SWIRE3 J104514.38+575708.8 (SWIRE 3-14)	10h45m14.4s	57d57m08.8s	1.7795	1/07/10, 3/17/11	31%
SWIRE3 J104632.93+563530.2 (SWIRE 3-18)	10h46m32.9s	56d35m30s	1.771	12/31/10	22.5%
SMM J030227.73 +000653.5 (SMM J03)	03h02m27.7s	00d06m52.0s	1.4076	1/4/11	16%
SWIRE4 J104427.52+584309.6 (SWIRE 4-5)	10h44m27.52s	58d43m09.6s	1.7560	1/24/11	36%
SWIRE4 J104656.46+590235.5 (SWIRE 4-15)	10h46m56.46s	59d02m35.5s	1.8540	3/16/11	30%
SDSS J120602.09+514229.5 (SDSS J12)	12h06m01.71s	51d42m27.6s	1.9985	3/17/11	21.5%

Notes. Average line-of-sight transmission is indicated by t_{los}. In the text, we refer to sources by their names in parentheses.

a standard chop-nod observing mode with a chopper frequency of 2 Hz, and a chopper throw of 30″. Calibration, including beam size, point-source coupling, and flux calibration, was determined by observations of Uranus, which is assumed to emit like a blackbody with temperatures 61 and 73 K within our 450 and 350 μm bands, respectively (Hildebrand et al. 1985). We spectrally flat-fielded our observations based on observations of a cold chopped source. Source and system parameters relevant for each observation are given in Table 1. The ZEUS/CSO beam size is 10.″5 at 350 μm and 11.″5 at 450 μm, and we estimate that typical pointing errors are less than 3″ and systematic calibration errors are less than 30%. The wavelength calibration is good to about half a pixel, or 100–160 km s^{-1}.

We observed six sources in [O I] 63 μm using the PACS spectrometer on board the *Herschel Space Observatory*. We observed using line scans in chop-nod mode with a small chopper throw. Each [O I] observation had a full integration time (including on and off source integration but not including instrumental overheads) of just under an hour (57.3 minutes), except for SWIRE 3-14, which is our faintest [C II] source, on which we integrated three times longer (172 minutes). We reduced the data using the standard pipeline in the Herschel Interactive Processing Environment (HIPE v10.3.0; Ott 2010), with minimal post-pipeline processing described in Section 4.1. Observations were carried out between 2012 May and October (ODs 1253, 1253, 1188, 1152, 1132, and 1118) covering ObsIDs 1342253587, 1342253586, 1342249495, 1342247784, 1342247131, and 1342246639, respectively. The [O I] line was observed in a seventh source, SDSS J12, as part of the open time program *Herschel Extreme Lensing Line Observations (HELLO)* by PI: Sangeeta Malhotra using the PACS chop-nod mapping mode (ObsID 1342246395.)

All sources except for SMM J03 lie in regions surveyed by either the HerMES or *SEDs and energetics of lensed UV-bright high redshift galaxies* projects from which we obtained photometric measurements. We conducted photometric observations of SMM J03 using the PACS blue and green cameras (which provide simultaneous red coverage resulting in observations at all three PACS wavebands—70, 100, and 160 μm). We took two scan maps with each camera, one at an orientation of 110 and one at 70 degrees with respect to the camera array for optimal spatial coverage and minimal CCD latency effects after cross stitching. Scans were performed at medium speed, with 3 arcmin scan legs, a cross scan step of 4 arcsec and a total of 10 scan legs. Total integration time including all four scan maps (without instrumental overhead) was six minutes. The observations are noted in the *Herschel* archive as ObsIDs 1342249159, 1342249158, 1342249157, and 1342249156 occurring on OD 1181.

3. NOTES ON OBSERVATIONS OF INDIVIDUAL SYSTEMS

Several of our sources were initially discovered as part of the *Spitzer* Wide-area InfraRed Extragalactic (SWIRE) survey (Lonsdale et al. 2003), which undertook deep photometric observations of several different fields. High-z candidates showed bumps in the 4.5 or 5.8 μm IRAC bands or the MIPS 24 μm band, indicating a redshifted stellar photospheric 1.6 μm feature or PAH emission at $z \sim 2$. Both types of features strongly suggest star formation. The 1.6 μm feature particularly selects for late type evolved stars, but it can be overwhelmed by a strong AGN contribution, so its presence in a FIR bright galaxy suggests star formation as the dominant power source (Farrah et al. 2006, 2008; Lonsdale et al. 2009; Huang et al. 2009; Desai et al. 2009).

All of our sources have MIR IRS spectra available that show strong PAH emission. The equivalent width (EW) of the 6.2 μm feature is often used as an AGN diagnostic. Sources with AGNs dominating the MIR have a hot dust continuum that can overwhelm PAH emission and suppress the EW. Although our sources have PAH equivalent widths reported in various published works, this measurement is highly sensitive to the details of the PAH spectrum fitting method used (especially in spectra with low signal-to-noise ratios and faint continuum as in our sources). Therefore, we cannot simply compare the published values of EWs in these sources, as they have been determined through diverse fitting methods.

Instead, we adopt the method described by Brandl et al. (2006) of integrating the PAH 6.2 μm feature above a spline-interpolated local continuum and using the spline continuum to determine the EW. This fit is performed in the rest frame

of the source. The continuum spline is fit to anchor points located in regions of the spectra straddling, but relatively unaffected by, the PAH emission features. In general, we used the same anchor points as those used by Stierwalt et al. (2013), but we inspected each spectrum individually and adjusted the anchor points where necessary to ensure no PAH emission was included. Since the resulting EW is especially sensitive to the exact integration range for the feature as well as the spline fit, we fit each spectrum several times, allowing the anchor points and integration range (nominally 5.94–6.56 μm for the 6.2 μm feature) to vary slightly, and used the standard deviation of these fits to characterize the error.

This method has been used by several authors, including Farrah et al. (2008), who included three of our sources among their sample (SWIRE 3-9, SWIRE 3-14, and SWIRE 3-18.) Below, we note the published EW for those three sources and our own measured EW for the other five sources. Cutoffs of $EW_{6.2} \sim 0.3$–$0.5\,\mu$m have been used to identify star-formation-dominated systems as those with greater EW, and AGN-dominated systems as those with smaller EW (Stierwalt et al. 2013; Díaz-Santos et al. 2013). The generally large (though uncertain) EWs we observe in our sample are, therefore, consistent with, though not strong evidence for, star-formation dominance over AGNs. We caution that the EWs for many of our sources have uncertainties of the order of the EW itself. For two of the sources published in Farrah et al. (2008), the uncertainty actually exceeds the EW. In these cases, the error is dominated by the uncertainty in identifying the faint continuum. Although we quote the published error, the true uncertainty is likely asymmetric skewing toward higher values since the continuum might easily be weaker than measured, buried underneath residual PAH emission, whereas a stronger continuum should be easier to detect and would lower the measured equivalent width.

SWIRE 4-15. IRS observations in Fiolet et al. (2010) (source L15) showed strong PAH features and indicated a (PAH determined) redshift, $z = 1.85 \pm 0.01$. We measure $EW_{6.2} = 0.97 \pm 0.60\,\mu$m. Photometry from *Spitzer* and SCUBA showing no significant presence of hot dust indicates an SF-D system with little to no contribution from AGNs.

SWIRE 4-5. IRS follow up of this source revealed strong PAH features and a redshift $z = 1.750 \pm 0.007$ (source L5; Fiolet et al. 2010). We measure $EW_{6.2} = 0.51 \pm 0.30\,\mu$m.

SWIRE 3-14. Farrah et al. (2008) find a PAH determined redshift of $z = 1.78 \pm 0.02$ and $EW_{6.2} = 1.26 \pm 1.52\,\mu$m.

SWIRE 3-9. Another SWIRE source suspected of being at $z \sim 2$, the MIR spectrum acquired by Farrah et al. (2008) showed this to have strong PAH features with a gentle continuum slope characteristic of an SF-D system, with no contribution from an AGN. They find a PAH derived redshift of $z = 1.71 \pm 0.02$ and $EW_{6.2} = 1.88 \pm 2.14\,\mu$m.

SWIRE 3-18. This source was selected for MIR spectral follow up by Farrah et al. (2008). Its MIR spectrum shows strong PAH features indicative of SF dominance. Farrah et al. (2008) find $EW_{6.2} = 3.96 \pm 1.49\,\mu$m. Prior to our [C II] detection, only a PAH determined redshift of $z = 1.76 \pm 0.02$ had been established. Our [C II] detection refines this to 1.771. Although it has been observed with IRS, little other data is known for this source. Our interest in it arose too late to include it in our [O I] *Herschel* survey.

SMM J03. Based on optical and UV lines probing the ionized gas, SMM J03 is thought to have an AGN component (Swinbank et al. 2004; Takata et al. 2006). Looking at the UV spectral diagnostics along with the bolometric luminosity, however, Chapman et al. (2005) found that the AGN contributes insignificantly to the overall luminous energy. We, therefore, consider it tentatively to be SF-D, with a potential minor contribution from an AGN. This is a well-studied submillimeter galaxy (SMG) with extensive photometry available in the literature in the optical, NIR, and radio regime. Rest frame optical spectroscopy reveals a redshift of $z = 1.4076 \pm 0.0002$ (Swinbank et al. 2004). We measure $EW_{6.2} = 0.41 \pm 0.28\,\mu$m.

SDSS J12 ("The Clone"). This is a UV bright lensed source with a magnification ~27 (Lin et al. 2009). It was discovered as the counterpart to the lensing galaxy at $z = 0.4$ in the Sloan Digital Sky Survey (SDSS). An analysis of rest frame optical lines, [O III], Hβ, [N II], and Hα by Hainline et al. (2009a) found SDSS J12 to share characteristics of local star-forming systems, but with stronger ionized emission, indicating particularly vigorous star formation. MIR follow up by Fadely et al. (2010) showed strong PAH emission. SDSS J12 shows strong [S IV] in emission and has a steeply rising MIR continuum. Both of these features may be associated with AGN presence, however, based on the strong PAH features and lack of other highly ionized lines such as [Ne VI] in the MIR spectrum Fadely et al. (2010) conclude that AGN contribution is minimal. We measure $EW_{6.2} = 0.47 \pm 0.16\,\mu$m. We consider it tentatively to be SF-D with possible AGN contribution. Several spectral lines observed in emission from SDSS J12 have indicated redshifts in the range $z = 1.9967$–2.0026 (Lin et al. 2009; Hainline et al. 2009a).

MIPS 22530. This source was selected as a potential $z \sim 2$ galaxy from the Spitzer Extragalactic First Look Survey (XFLS) based on its 24/8 μm flux ratio, which indicated strong redshifted PAH emission (Yan et al. 2007). Multiwavelength analysis by Sajina et al. (2008) finds a borderline indication of AGN-powered radio emission, but shows a lack of AGN presence in optical lines. This, along with strong PAH emission, leads them to conclude that it is an SF-D system. We measure $EW_{6.2} = 0.49 \pm 0.24\,\mu$m. We consider it to be SF-D with a possible modest AGN contribution. Keck spectroscopy by Yan et al. (2007) reveal an optical redshift of $z = 1.9511$.

4. RESULTS AND ANALYSIS

Here we give an overview of the results that define several aspects of our sample as a whole, followed by analyses of the individual systems.

4.1. Line Spectra

We have detected eight $1 < z < 2$ sources in [C II] with ZEUS, representing a significant increase in the population of sources detected in this line during the epoch of peak star formation. In Figure 1, we show the [C II] spectra from these eight sources. Although some of our sources may be lensed, the apparent [C II] luminosities span a range of 0.73–$5.44 \times 10^{10} L_{\odot}$.

The [O I] spectra for the six sources we observed in our *Herschel* PACS [O I] survey plus one observed by Sangeeta Malhotra (reduced here from archival data,) are plotted in Figure 2. The [O I] spectra were reduced through standard methods using HIPE. In post-processing we rebinned them to resolutions ~120–350 km s^{-1} and fit a linear baseline to channels with no line emission. Line fluxes are tabulated in Table 2.

The [O I] line is clearly detected in six of the seven sources, and marginally detected in SWIRE 4-5 (discussed in

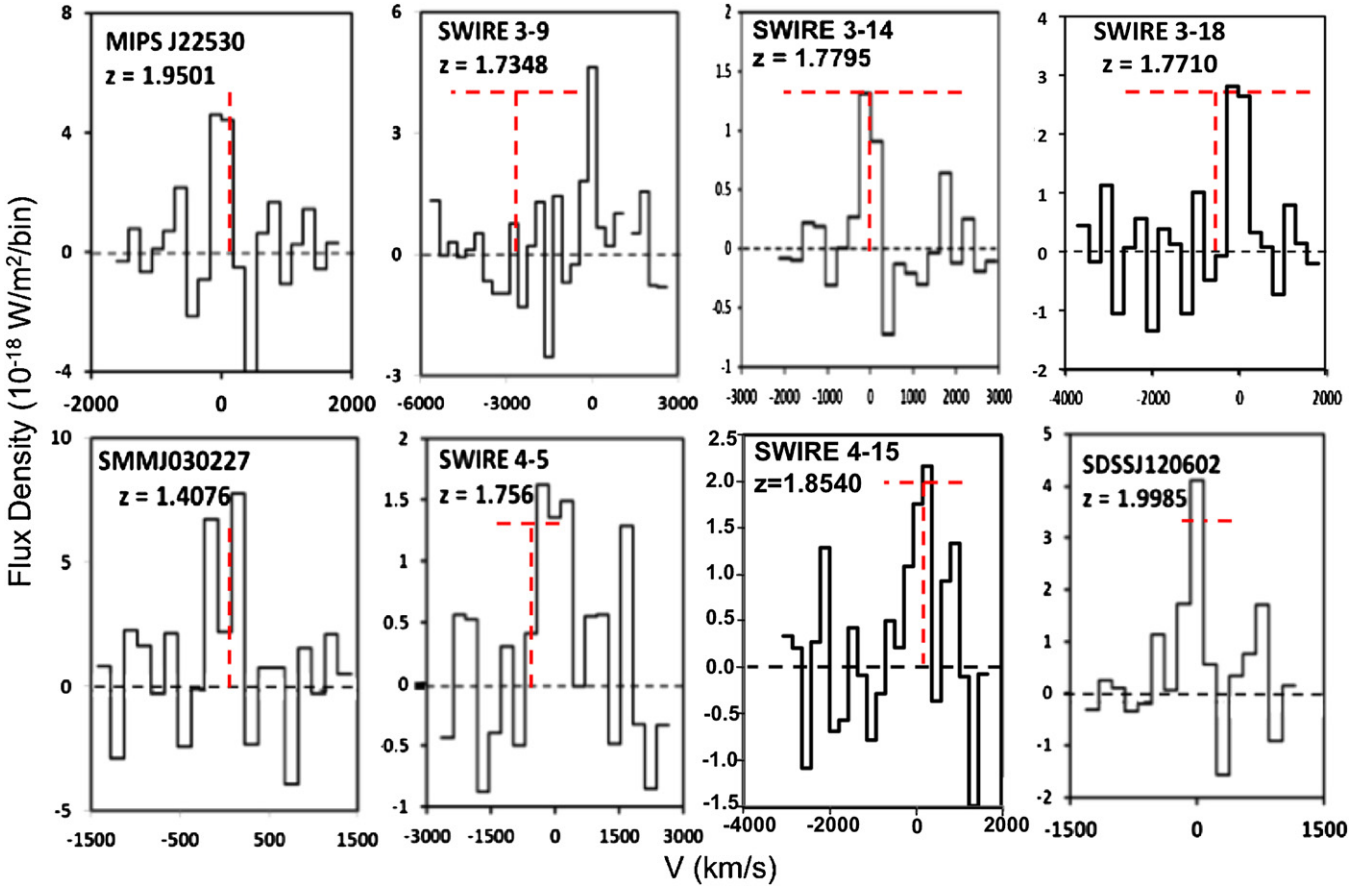

Figure 1. ZEUS/CSO [C II] spectra of the eight galaxies reported here. Each spectral bin is one resolution element of the spectrometer and is statistically independent from its neighbors. The velocity scale is centered on the [C II] line center. Red dashed lines indicate literature redshift values and uncertainty range where available. Note that the literature redshifts for MIPS J22530 and SMM J03 do not include uncertainty ranges, while for SDSS J12 a range of possible redshifts exist with no clearly preferred value.

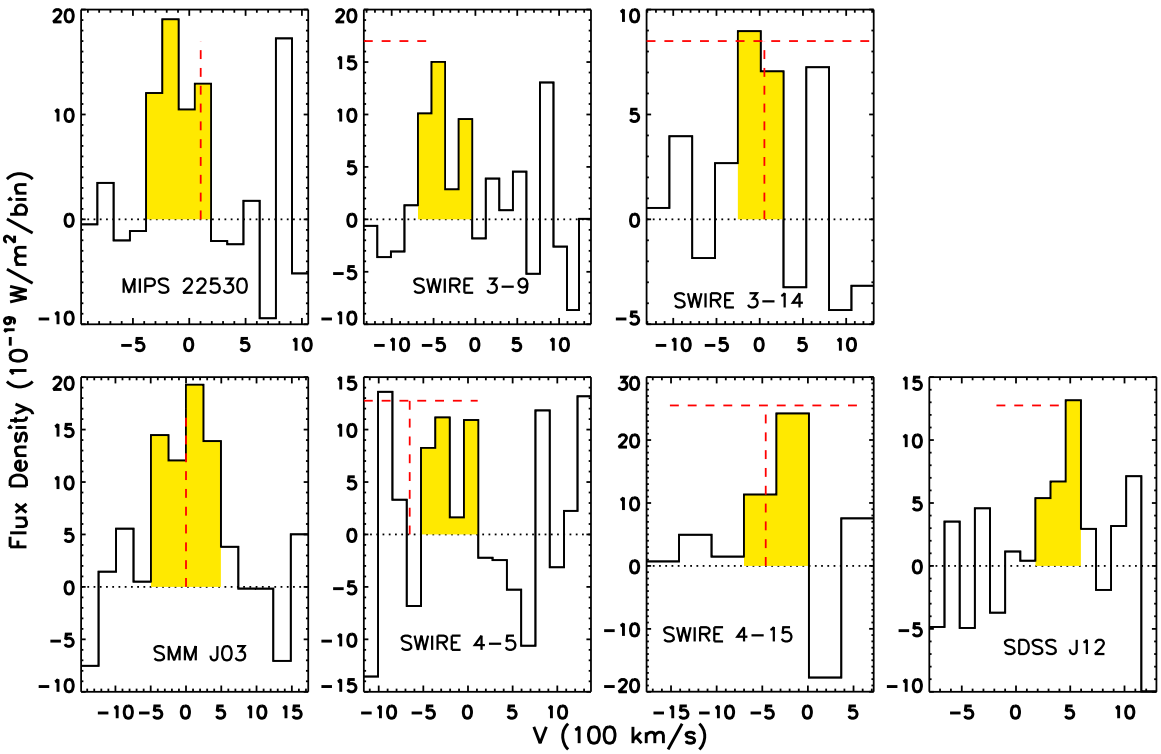

Figure 2. PACS [O I] spectra from the six sources observed in our *Herschel* program and SDSS J12, observed by Sangeeta Malhotra (PI). SWIRE 3-18 was not observed. Velocities are with respect to our [C II] line center. The region shaded in yellow indicates the area integrated to determine line flux. Red dashed lines indicate redshifts from the literature, as in Figure 1.

Table 2
Fine Structure Lines and SED Properties

Source	$\log(\frac{L_{\rm FIR}}{L_\odot})$	$\frac{F_\nu(70)}{F_\nu(100)}$	$F_{[\rm C\,II]}$	$F_{[\rm O\,I]}$	$\frac{F_{[\rm O\,I]}}{F_{[\rm C\,II]}}$	$\frac{L_{[\rm C\,II]}}{L_{\rm FIR}}$	$\frac{L_{[\rm O\,I]}}{L_{\rm FIR}}$
			(10^{-18} W m^{-2})				
MIPS 22530	12.69 ± 0.04	$1.01\pm^{0.10}_{0.05}$	9.3 ± 2.1	5.4 ± 1.1	0.59 ± 0.18	(1.4 ± 0.3)E -2	(8.0 ± 1.8)E −3
SWIRE 3-9	12.59 ± 0.15	$1.01\pm^{0.26}_{0.29}$	6.4 ± 1.4	3.75 ± 0.78	0.59 ± 0.18	(8.9 ± 3.7)E -3	(5.2 ± 2.1)E −3
SWIRE 3-14	12.21 ± 0.13	$0.61\pm^{0.15}_{0.16}$	2.3 ± 0.4	1.60 ± 0.48	0.69 ± 0.24	(8.3 ± 2.9)E -3	(5.7 ± 2.4)E −3
SWIRE 3-18	12.13 ± 0.13	$0.61\pm^{0.15}_{0.17}$	5.5 ± 1.0	···	···	(2.3 ± 0.8)E -2	···
SMM J03	12.58 ± 0.03	$1.19\pm^{0.08}_{0.09}$	16.9 ± 3.5	5.97 ± 0.86	0.353 ± 0.089	(1.5 ± 0.3)E -2	(5.11 ± 0.82)E −3
SWIRE 4-5	11.73 ± 0.19	$0.44\pm^{0.27}_{0.03}$	4.5 ± 1.1	3.2 ± 1.0	0.72 ± 0.28	(4.7 ± 2.4)E -2	(3.3 ± 1.8)E −2
SWIRE 4-15	12.36 ± 0.15	$0.85\pm^{0.25}_{0.18}$	5.0 ± 1.3	3.55 ± 0.90	0.71 ± 0.26	(1.4 ± 0.6)E -2	(9.9 ± 4.3)E −3
SDSS J12	12.54 ± 0.03	$1.30\pm^{0.06}_{0.15}$	5.6 ± 1.4	2.52 ± 0.47	0.45 ± 0.14	(1.3 ± 0.3)E -2	(5.6 ± 1.1)E −3

Notes. For the full set of SED properties that we use to compare our sample to other data sets and models, see Table 7 in the Appendix. We summarize them here since many of the properties are highly correlated and encapsulate similar information (e.g., $F_\nu(70)/F_\nu(100)$ and $F_\nu(60)/F_\nu(100)$).

Section 4.5). In a few sources, we observe offsets from the [C II] line velocity by ∼250 km s^{-1}. Both the velocity resolution and signal-to-noise ratios in our [C II] spectra are modest, however, and a slight calibration error could introduce a velocity error of ∼200 km s^{-1}; thus, the offset between [O I] and [C II] is acceptable and does not require a physical explanation.

4.2. Photometry and SEDs

The photometry from our PACS program and the literature is compiled in Table 6 in the Appendix. To estimate FIR properties such as $L_{\rm FIR}$ and the 70–100 μm flux density ratio in a uniform manner (Table 2), we fit star formation SED models from Dale & Helou (2002) to available photometry. The SED library consists of a set of 64 templates, each described by a different power-law distribution of dust mass over heating intensity, parameterized by α:

$$dM_d(U) \propto U^{-\alpha} dU, \quad (1)$$

where $M_d(U)$ is the dust mass heated by the radiation field at intensity U. Higher (lower) values of alpha correspond to SEDs with dust distributions skewed toward cooler (warmer) temperatures averaged over the galaxy. The total luminosity of the system is a free parameter, which can be scaled up or down.

We compared each template against available photometry in the 60–1200 μm range weighted by error and formed likelihood functions to determine several global properties including $L_{\rm FIR}$, 70/100 and 60/100 μm flux density ratios along with their corresponding 68 percentile likelihood range.[11] The best-fit SED for each of our sources is shown in Figure 3.

The SED templates fit our observed photometry well. In Figure 4, we compare the sources' luminosities and dust temperatures (indicated by the 60/100 μm flux ratio) with those of local sources (Brauher et al. 2008). In local sources there is a weak trend of increasing dust temperature with increasing luminosity. Our sources span the full range of dust temperatures seen in local sources. The three sources from our sample with marginal evidence for AGN contribution fall to the right, hot dust temperature side of the plot. One revealing aspect of this figure is that our sources with the lowest dust temperatures have luminosities many times greater than the equivalent dust temperature sources in the local universe. No corrections have been made for gravitational lensing effects, though in our sample only one source, SDSS J12, is known to be gravitationally lensed. Lin et al. (2009) find a magnification factor of 27.

The occurrence of highly luminous systems with cooler dust peaks at high-z is well established (Elbaz et al. 2011; Symeonidis et al. 2013), and further confirms the general findings that SF-D systems at high- z can be represented as scaled up local star-forming systems. The conditions of star formation in our $z = 1$–2 sources give rise to cool dust peaks similar to those of local normal or LIRG class galaxies, but scaled up spatially to account for ULIRG (or LIRG in the case of SWIRE 4-5) luminosities.

To place these sources in context with the larger population of galaxies at these redshifts, we consider their bulk star formation rates (SFRs) and stellar masses. The TIR luminosity, largely emitted by dust heated by young stars, is a convenient star formation tracer with a long history of use. We use the TIR–SFR relationship established by Kennicutt (1998) and adapted by Nordon et al. (2010) to adjust for a Chabrier (2003) IMF:

$$\frac{\rm SFR}{M_\odot {\rm yr}^{-1}} = \frac{L_{\rm TIR}}{L_\odot} 1.015 \times 10^{-10}. \quad (2)$$

Several methods of estimating galaxy stellar mass based on various photometric recipes have been used in local galaxies. These methods are generally based on galaxy SED modeling and rely on multiple optical/NIR measurements to break degeneracies in star formation history. A crude but effective estimation can be arrived at based solely on the rest frame galaxy luminosity at ∼2 μm, a wavelength which yields nearly constant mass to luminosity ratios that are less dependent on star formation histories (de Jong 1996; Bell et al. 2003). The effectiveness of the 2 μm luminosity for the purpose of estimating stellar masses has already been demonstrated at $z \sim 3$ using IRAC 8 μm measurements (Magdis et al. 2010), and here we extend the approach to $z \sim 1.8$ where the appropriate rest wavelength coincides with the IRAC 5.8 μm band. We take this IRAC band to represent the rest frame 2 μm flux and directly use the relationship established by Magdis et al. (2010):

$$\log(M_*/M_\odot) = 2.01(\pm 0.65) - 0.35(\pm 0.03) \times M_{2\mu{\rm m}}, \quad (3)$$

where $M_{2\mu{\rm m}}$ represents the rest frame 2 μm absolute magnitude. As is clear from the uncertainty in the coefficients to Equation (3), the resulting stellar mass estimate should only be taken as an order of magnitude approximation. Nonetheless, we are reassured that it is an appropriate order of magnitude estimate by the examples of SWIRE 4-5 and SWIRE 4-15. Both of

[11] In most sources, 24 μm observations are also available. In the rest frames of our sources, 24 μm observations probe the PAH-dominated MIR and have little bearing on the FIR properties that we hope to constrain with SED fits. Therefore, although we plot these data in the SEDs, we do not use them in performing the fit.

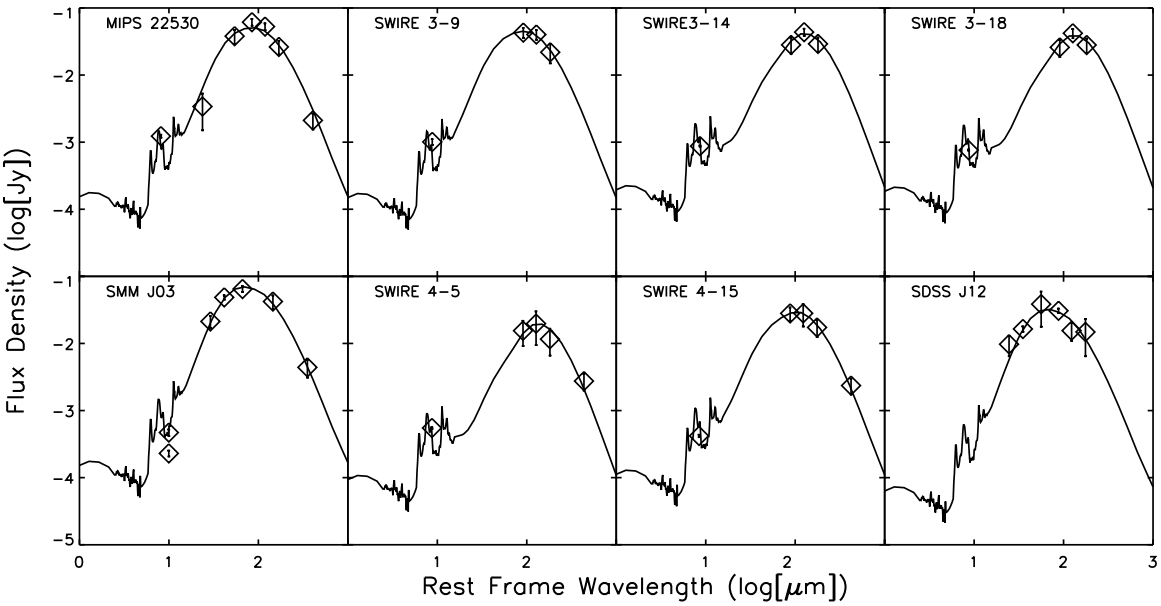

Figure 3. Best-fit SED model from the library of Dale & Helou (2002) for each of our sources. Photometry (diamonds) is listed in Table 6. Data from 24 μm observations is plotted but not used in the SED fit.

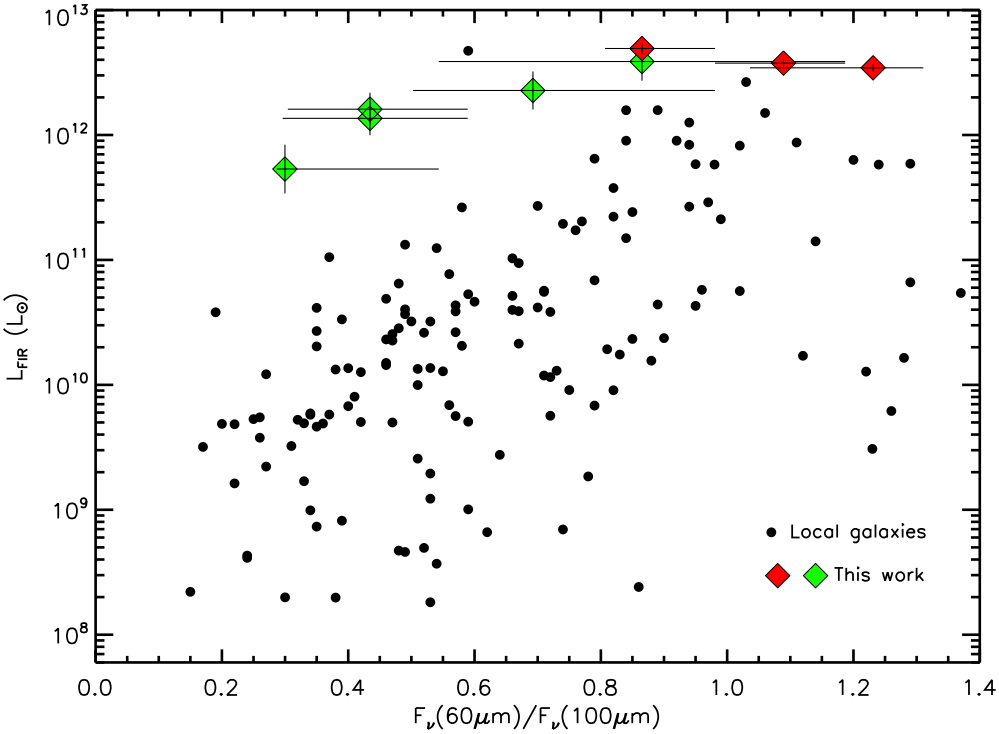

Figure 4. $L_{\rm FIR}$ vs. $F_\nu(60)/F_\nu(100)$. Local sources are from the sample of Brauher et al. (2008). Our sources are indicated by diamonds. Although we believe the luminosity in all of our sample is dominated by star formation, we note that the three sources with marginal evidence for AGNs in the literature (SMM J03, SDSS J12, and MIPS 22530—noted by red diamonds) tend to have hotter dust temperatures than those with no indication of an AGN present (green diamonds). All of our sources have significantly larger luminosities than average local galaxies of similar F_{60}/F_{100} values. No corrections for gravitational lensing have been made. Magnification corrections (if applicable and known) affect luminosity only and would bring our galaxy luminosities closer to those of the local galaxy group.

these sources were examined in Fiolet et al. (2009), where careful multi-band photometric stellar estimates yielded 1.36 and $3.21 \times 10^{11}\ M_\odot$, respectively. Our simple stellar mass estimates of 1.35 and $2.05 \times 10^{11}\ M_\odot$ are in satisfactory agreement.

In Table 3, we note the derived SFRs and stellar masses of the seven sources for which there are IRAC 5.8 μm measurements and, in Figure 5, we overplot these data on the sample presented by Fiolet et al. (2009). Although our sample consists of massive, highly star-forming sources, their relative mass and SFRs (or, alternatively, their specific star formation rates) follow the trend exhibited by most galaxies, very close to the stacked results of the Fiolet sample. In other words, our sample falls on the galaxy "main sequence" (Noeske et al. 2007).

4.3. [C II], [O I] and the FIR Continuum

In Figure 6, we plot [C II]/FIR versus $L_{\rm FIR}$. While the absolute [C II] line luminosity and $L_{\rm FIR}$ may be amplified by gravitational lensing, the FIR continuum and [C II] emitting regions will

Table 3
Stellar Mass and SFR Estimates for Sources with IRAC Measurements

Source	$\log\left(\frac{\mathrm{SFR}}{M_\odot \mathrm{yr}^{-1}}\right)$	$F_{\mathrm{IRAC5.8}}$ (mJy)	M_* ($10^{11} M_\odot$)
MIPS 22530	2.96 ± 0.04	(4.3 ± 1.0)E-2	1.4
SWIRE 3-9	2.83 ± 0.16	(1.12 ± 0.06)E-1	2.5
SWIRE 3-14	2.55 ± 0.08	(7.00 ± 0.35)E-2	1.8
SWIRE 3-18	2.49 ± 0.09	(6.80 ± 0.34)E-2	1.7
SMM J03	2.85 ± 0.03	(8.16 ± 0.83)E-2	1.2
SWIRE 4-5	2.11 ± 0.15	(5.36 ± 0.46)E-2	1.3
SWIRE 4-15	2.62 ± 0.15	(7.63 ± 0.35)E-2	2.1

generally be cospatial in SF-D galaxies, so that the [C II]/FIR ratio is not very susceptible to differential magnification (Serjeant 2012). Local sources (black, white, and gray circles) clearly illustrate the historically reported [C II] deficit, showing [C II]/FIR decreasing with increasing L_{FIR} (largely established by the works Malhotra et al. 2001; Luhman et al. 2003).

Many of our SF-D sources from this work show [C II] emission with [C II]/FIR ratios in excess of 1%. Although such high [C II]/FIR is unusual, it is not unheard of. In Section 4.5, we show that these observations push models for PDR origins of the [C II] emission to their limits. There are previous examples of sources with high [C II]/FIR ratios. For example, H-ATLAS SDP 81 (Valtchanov et al. 2011), at $z \sim 2.3$ and the nearby spiral galaxy M51 (Nikola et al. 2001), both show [C II]/FIR ~ 0.01. Spatially resolved studies of star-forming regions in M33 show [C II]/FIR luminosity ratios ranging from 0.001 up to 0.04 (Mookerjea et al. 2011). Assuming the [C II] and FIR arise in PDRs, [C II]/FIR $\sim 1\%$ indicates $G \sim 100$ implying that the star formation regions in our sources must be very extended given their large FIR luminosities (Stacey et al. 2010b). There are, however, hints that other mechanisms may sometimes contribute to [C II] emission. Several resolved regions of Stephan's Quintet, for instance, have extremely high [C II]/FIR ratios as a result of shocked PDRs (Appleton et al. 2013).

Considering the [C II]/FIR ratio in context with the FIR dust temperature, in Figure 7, we note that both local sources and our high redshift sample shows the [C II]/FIR ratio tending to decrease with increasing $F_\nu(60)/F_\nu(100)$. Our sample, however, lies above the trend observed in local galaxies, and in the case of SWIRE 4-5 approaches the [C II]/FIR and dust temperature seen in regions of Stephan's Quintet. Although the uncertainties on the FIR colors in our SED fits are large, it is also worth noting that MIPS 22530, SDSS J12, and SMM J03, the three sources that have tentative evidence for AGNs in the literature, have higher $F_\nu(60)/F_\nu(100)$ ratios, consistent with the presence of an AGN contributing to a hot dust component.

The [O I] 63 μm line is the other primary coolant in PDRs. As we show in Figure 8, [O I] traces out a similar line to IR continuum deficit in local sources as the infrared luminosity increases. Although less pronounced than what we see in the [C II] line, our sources again show enhanced line emission compared to local sources of similar luminosity. Our sources have $L_{[\mathrm{O\,I}]}/L_{\mathrm{IR}}$ ratios similar to the galaxy sample of Coppin et al. (2012). Their sample was a set of Large Apex Bolometer Camera (LABOCA) submillimeter selected galaxies with spectroscopic redshifts. Based on their FIR photometry and [O I] line, Coppin et al. (2012) concluded their sample was most like scaled up "normal" star bursting systems with spatially extended star formation, rather than merging ULIRGs.

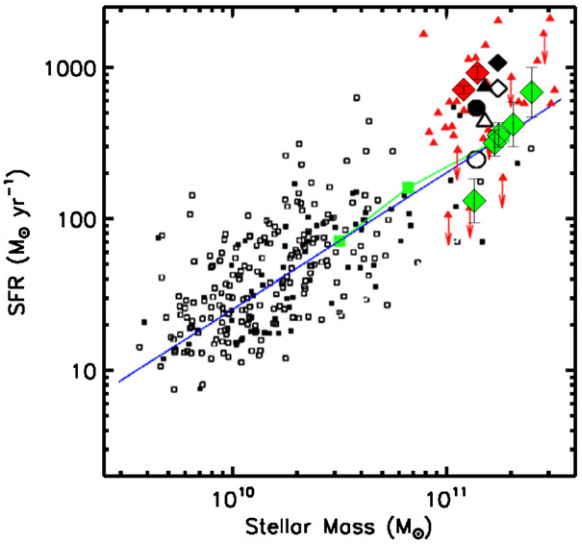

Figure 5. SFR vs. stellar mass. Adapted from Figure 6 of Fiolet et al. (2009). The SFRs and stellar masses of our sample, represented by filled green and red diamonds, are determined by L_{FIR} and the IRAC 5.8 μm flux density. One source, SDSS J12, is not included because no IRAC 5.8 μm data is available. The x error bars have been suppressed for clarity because we only have order of magnitude stellar mass estimates. Red triangles represent the $z \sim 2$ sources presented by Fiolet et al. (2009), large black symbols represent stacked subsets of the Fiolet sample, small black symbols represent $z \sim 2$ sources from Daddi et al. (2007). Green squares trace the average trend in GOODS-N. The "main sequence" of galaxies stands out as a strong correlation of SFR and stellar mass, clustering about the blue line.

Due to the higher critical density and excitation potential of [O I] 63 μm compared to [C II], higher [O I]/[C II] ratios correspond to more compact star-forming regions and are correlated with warmer FIR colors (Malhotra et al. 2001; Díaz-Santos et al. 2013). From Figure 9 we see that our high-z sample spans the full range of FIR color seen in local galaxies, but even in our sources with hot dust temperatures the [O I]/[C II] ratios are modest, similar to cool star-forming galaxies in the local universe. Possibly those sources in our sample with large $F_\nu(60)/F_\nu(100)$ values have a hotter dust component related to a potential AGN contributing to the 60 μm continuum, while cool dusty PDRs contribute the bulk of the [O I] and [C II] emission.

4.4. PAHs

PAHs are the main source of photo-ejected electrons for neutral PDR gas heating (Weingartner & Draine 2001). As a simple diagnostic of heating (traced by PAHs) versus cooling (traced by [C II]), the ratio of [C II] to PAH emission is of interest much in the same way as the [C II]/FIR ratio. The PAH features in several of our sources have been examined in other works, however, PAH fluxes are sensitive to the fitting method used. Therefore, in order to obtain a uniform data set we fit the MIR spectra ourselves using PAHFIT (Smith et al. 2007). The fitted spectra are shown in Figure 10 and the fluxes are listed in Table 4. Most of the PAH spectra were acquired through the Cornell AtlaS of *Spitzer*/IRS Sources (CASSIS)[12] version 6 using the optimal extraction for point sources. Since MIR spectra contain overlapping PAH and silicate features, it is difficult to independently estimate uncertainties. To get the best estimate, we fit each spectrum repeatedly, adding a Gaussian distributed random error to each spectral data point in proportion to each

[12] The Cornell Atlas of *Spitzer*/IRS Sources (CASSIS) is a product of the Infrared Science Center at Cornell University, supported by NASA and JPL.

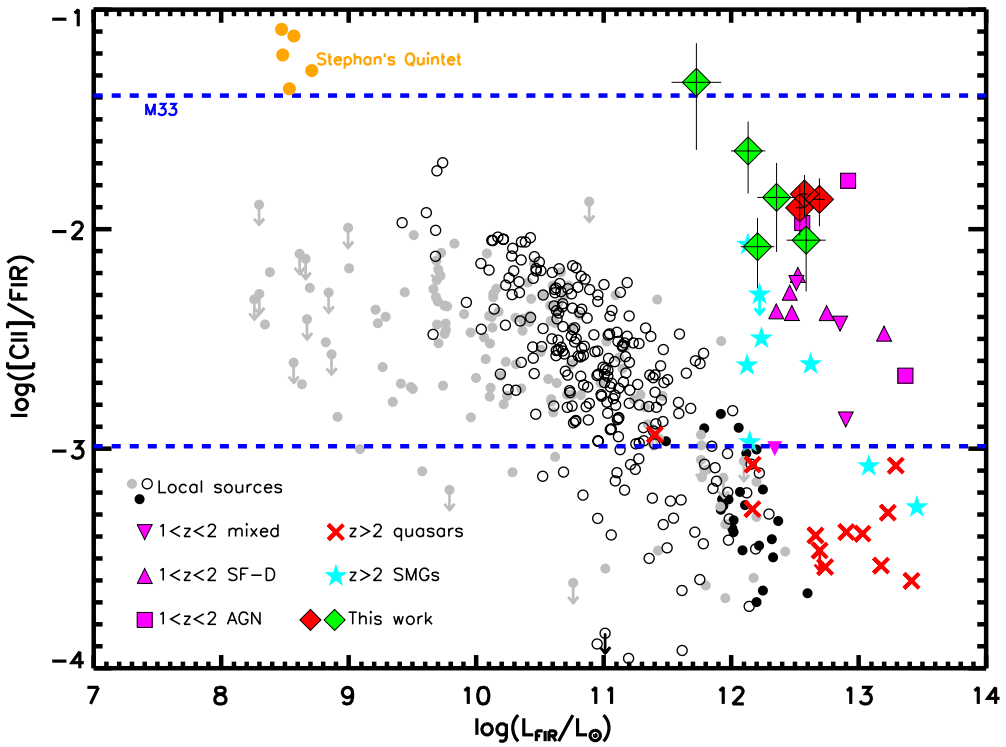

Figure 6. Observed [C II]/FIR vs. $L_{\rm FIR}$. Our sample is shown as in previous figures. We have also included local sources from Brauher et al. (2008; gray circles), the GOALS sample (Armus et al. 2009; Díaz-Santos et al. 2013; open circles), and Farrah et al. (2013; black filled circles). Magenta $1 < z < 2$ sources are from Stacey et al. (2010b) (updated by Ferkinhoff et al. (2014) and S. Hailey-Dunsheath (in preparation), and several high redshift SMGs and QSOs are from (Pety et al. 2004; Marsden et al. 2005; Maiolino et al. 2005, 2009; Ivison et al. 2010; Valtchanov et al. 2011; De Breuck et al. 2011; Swinbank et al. 2012; Wagg et al. 2012; Gallerani et al. 2012; Venemans et al. 2012; Willott et al. 2013; Wang et al. 2013; Riechers et al. 2013). We also note shock-affected regions from Stephan's Quintet (Appleton et al. 2013) (orange circles,) and the ratios spanned by star-forming regions within M33 (Mookerjea et al. 2011).

point's error bar. We fit each spectrum a hundred times and report the mean PAH fluxes and their standard deviations.

In all of our sources, only a portion of the full PAH spectrum is accessible (usually the range covered by the IRS long–low (LL) module.) At $z \sim 1.8$ this covers wavelengths of 5–14 μ m. Although this range misses several PAH features, based on Figure 6(d) in Croxall et al. (2012), we can estimate the total PAH emission as

$$\mathrm{PAH_{tot}} \approx \frac{8.47\mathrm{PAH_{11.2}}}{1.73 - 0.197\mathrm{PAH_{7.7}/PAH_{11.2}}}. \quad (4)$$

This PAH estimator uses both the 7.7 and 11.2 μ m features, representative of the ionized and neutral PAH species, respectively.

We present $\mathrm{PAH_{tot}}$ in Table 4, but note that the PAH flux ratio in the denominator of Equation (4) can lead to very large errors, and in some cases the flux in the PAH features we observe is greater than the lower uncertainty bound on $\mathrm{PAH_{tot}}$. Where this is the case, we use the observed summed flux in PAH features between 6.2 and 11.2 μm to more tightly constrain the lower bound of the total PAH flux. Therefore, when we consider the [C II]/PAH ratio we often have asymmetric error bars. In Figure 11, we plot the [C II]/PAH ratio with respect to the FIR color and compare to the subgalactic sample of star-forming regions from Croxall et al. (2012). Our sources demonstrate a [C II] excess with respect to PAH emission compared to the subgalactic local star-forming regions. We have also revisited the star-forming sources with available PAH spectra from Stacey et al. (2010b) and included their [C II]/$\mathrm{PAH_{tot}}$ values, which span a similar range. Croxall et al. (2012) found a negative

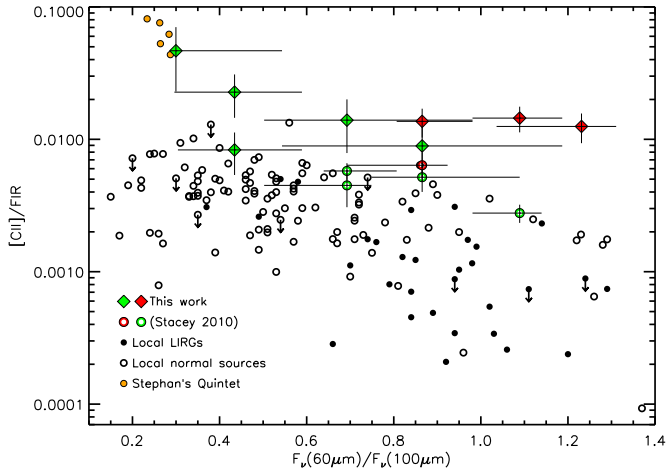

Figure 7. Observed [C II]/FIR ratio as a function of the 60–100 μm flux density ratio. Local sources are from the Brauher et al. (2008) sample and are plotted as small open circles (normal galaxies) and filled black circles (LIRGs). Our sources and Stephan's Quintet are plotted the same as in previous figures. We also plot sources revisited from Stacey et al. (2010b) as large open circles. As with the sample from this work, the Stacey et al. (2010b) sources are marked in green for star formation dominant, and red for a system with uncertain AGN contribution (SMM J22471.) Although the uncertainty in the dust temperature of our sources is large, our sample tends to decrease in [C II]/FIR as their dust temperature increases similar to the trend in local galaxies, though our sample lies above the local trend. Asymmetric error bars span the 68.27% most likely range of 60/100 μm flux ratios in our SED fits.

correlation between [C II]/PAH and $F_\nu(70)/F_\nu(100)$ (as well as the $\mathrm{PAH_{7.7}/PAH_{11.2}}$ flux ratio.) This trend is not apparent in our sources, though the large error bars in $F_\nu(70)/F_\nu(100)$ do not allow us to rule out a similar trend.

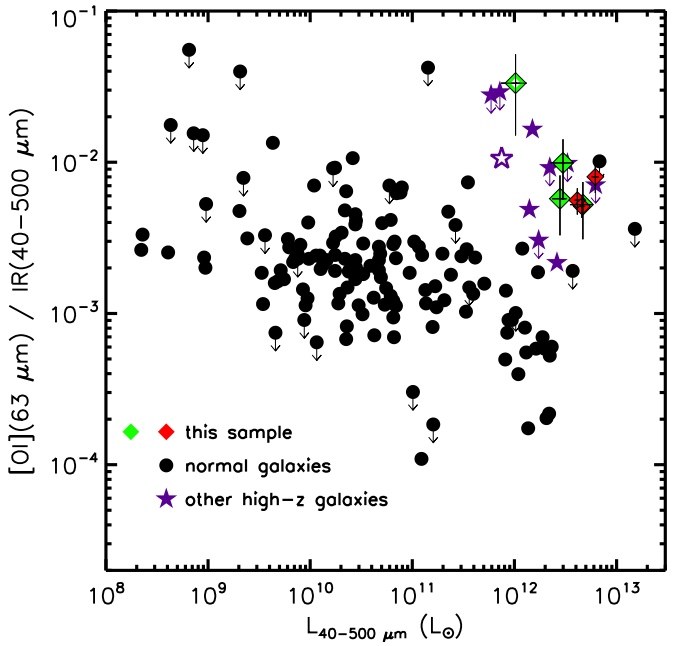

Figure 8. Observed [O I] 63 μm/IR ratio vs. L_{IR}. To compare to the sample of Coppin et al. (2012), here we have used the infrared continuum range of 40–500 μm. Local sources (black circles) are from the compilation by Graciá-Carpio et al. (2011) which includes additional data from Colbert et al. (1999), Malhotra et al. (2001), Negishi et al. (2001), Luhman et al. (2003), Dale et al. (2004), and Brauher et al. (2008). Literature high redshift sources are denoted with purple stars (Coppin et al. 2012; Brauher et al. 2008; Ivison et al. 2010; Valtchanov et al. 2011; Sturm et al. 2010). Our sample is marked with diamonds as before. In our sample and also the sample from Coppin et al. (2012), there is one tentative [O I] detection that we mark with an open diamond and star, respectively.

4.5. PDRs

Fine structure [C II] and [O I] line emission in normal star-forming galaxies is generally explained in a PDR paradigm. To explore PDRs as sources of the observed line emission, we use the PDR toolbox (Pound & Wolfire 2008; Kaufman et al. 2006) to analyze our source properties. The PDR models provide estimates of several PDR gas cooling lines over a large phase space of density, n (cm^{-3}), and FUV irradiation, G_0. For the majority of our sources the useful constraints on PDR characteristics are based on the [O I]/[C II] ratio, which rises with increasing density and G_0, and either [C II]/IR or ([C II]+[O I])/IR, which characterizes the gas heating efficiency and decreases with G_0.[13] The output of the PDR models is the intrinsic line emission from the PDR. Before we can interpret the model outputs in terms of physical conditions, we need to translate between the observed and intrinsic line emission. As a simple model, we assume a dual-slab molecular cloud geometry in which both faces of externally irradiated molecular clouds harbor PDRs. Cloud-to-cloud velocity variation generally allows us to observe emission from multiple clumps without optical depth effects. The [O I] line, however, is often optically thick on the surfaces of individual molecular clouds (Stacey et al. 1983), so we will only detect [O I] emission from the front surfaces of clouds. To account for this, we multiply the observed [O I] flux by two to match the plane parallel models in the PDR toolbox. Geometry and velocity dispersions may vary, but results from this simple approximation are generally successful at characterizing observations on a galactic scale (e.g., Malhotra et al. 2001; Vasta et al. 2010).

[13] The infrared continuum used in the PDR toolbox corresponds to the wavelength range of 30–1000 μ m (Farrah et al. 2013).

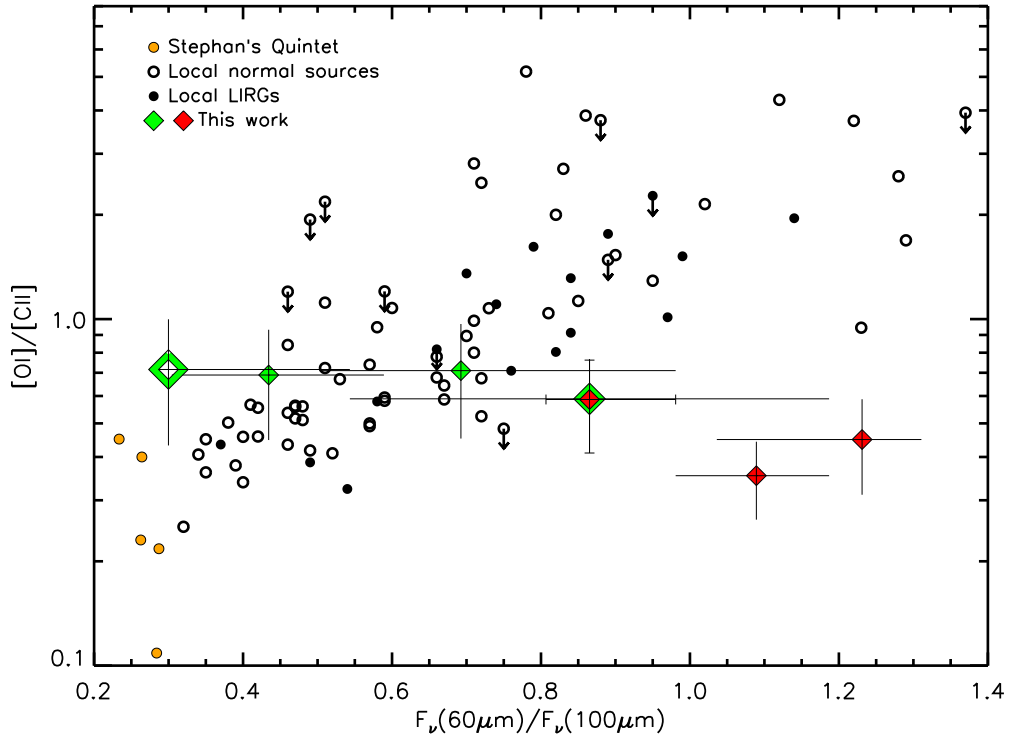

Figure 9. Observed [O I] 63 μm/[C II] line flux ratio as a function of the 60 to 100 μm color. Symbols are the same as in Figure 7 with the addition of an open diamond indicating our tentative [O I] detection of SWIRE 4-5. Note that SWIRE 3-9 and MIPS 22530 have the same line ratio and FIR color. We have enlarged the symbol for SWIRE 3-9 and added serifs to its error bars to differentiate the overlapping points, though they share the same line ratio error range. Local ULIRGs tend to have higher [O I]/[C II] ratios and warmer dust temperatures. The [O I]/[C II] ratios in our sample are similar to local normal sources. Even our sources with marginal AGN influence, which have warmer dust temperatures, have [O I]/[C II] ratios more similar to local normal galaxies rather than LIRGs.

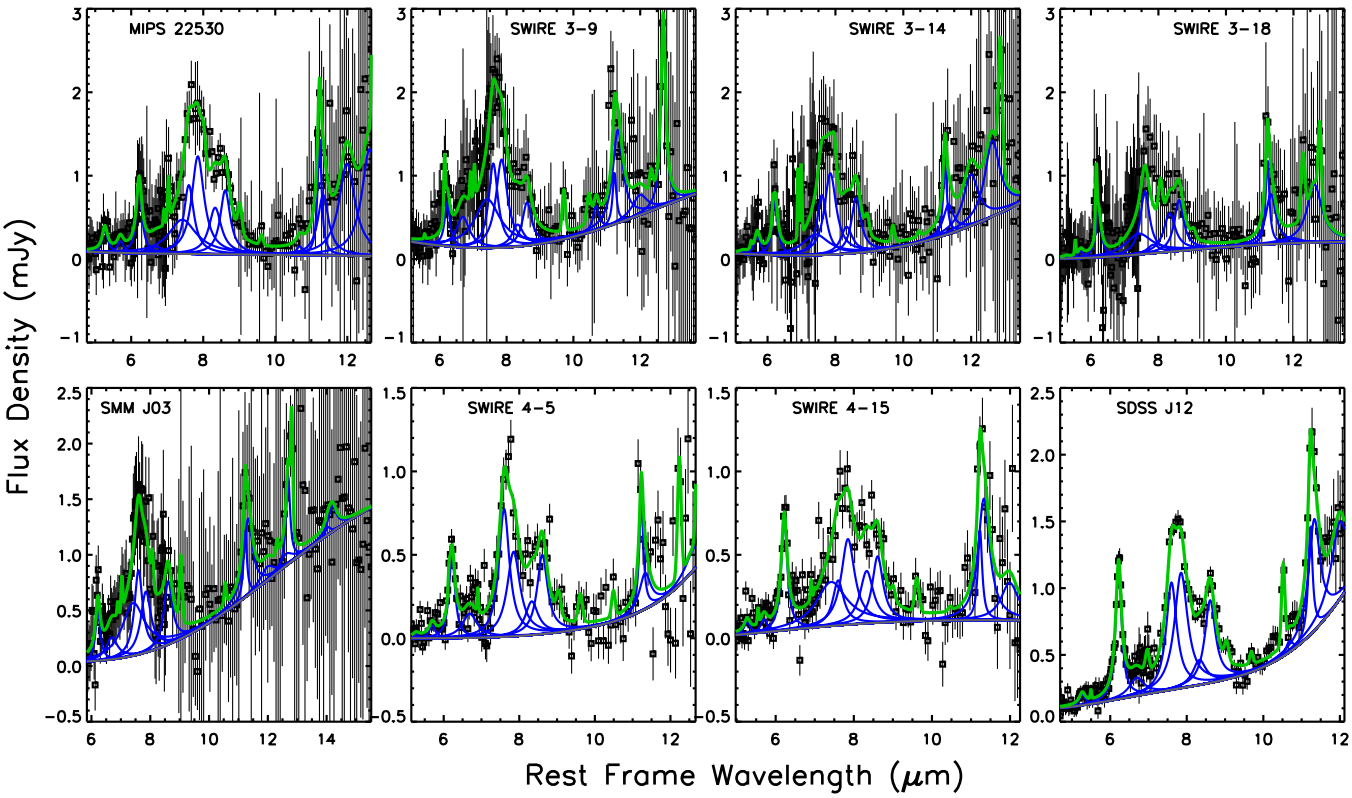

Figure 10. MIR IRS spectra fitted with PAHFIT (Smith et al. 2007). The green curve is the overall fit, blue curves are PAH contributions, and the underlying gray curve is the continuum fit by stellar and dust contributions. Sources of PAH spectra are noted in Table 4.

Table 4
PAH Features

Source	PAH Flux (10^{-18} W m^{-2})				(Equation (4))	[C II]/PAH$_{tot}$	Ref./AORkey
	6.2 μm	7.7 μm	8.6 μm	11.2 μm	PAH$_{tot}$		
MIPS 22530	6.3 ± 1.5	31.1 ± 3.3	5.7 ± 0.8	5.5 ± 1.9	75 ± 24	$0.12\pm^{0.07}_{0.07}$	AOR:11865856, 23632896
SWIRE 3-9	4.6 ± 1.3	39.2 ± 4.5	4.5 ± 2.0	7.1 ± 1.5	93 ± 21	$0.07\pm^{0.02}_{0.02}$	AOR:17414656
SWIRE 3-14	5.7 ± 1.3	24.9 ± 4.3	5.1 ± 1.9	3.7 ± 1.2	75 ± 65	$0.03\pm^{0.02}_{0.03}$	AOR:17415424
SWIRE 3-18	4.9 ± 2.3	15.5 ± 3.5	5.1 ± 1.6	5.0 ± 1.1	37 ± 6	$0.19\pm^{0.05}_{0.05}$	AOR:17416960
SMM J03	4.3 ± 1.3	31.3 ± 3.7	5.0 ± 1.9	6.2 ± 2.4	71 ± 14	$0.24\pm^{0.07}_{0.07}$	AOR:13983744, 14007040
SWIRE 4-5	4.1 ± 0.3	13.2 ± 0.6	3.7 ± 0.4	2.4 ± 0.4	31 ± 4	$0.14\pm^{0.04}_{0.04}$	(Fiolet et al. 2010)
SWIRE 4-15	5.3 ± 0.3	15.7 ± 1.5	3.1 ± 0.4	4.4 ± 0.5	36 ± 2	$0.17\pm^{0.04}_{0.04}$	(Fiolet et al. 2010)
SDSS J12	7.6 ± 0.3	17.0 ± 0.8	4.4 ± 0.3	5.3 ± 0.6	40 ± 2	$0.14\pm^{0.03}_{0.03}$	(Rujopakarn et al. 2012)
(Stacey et al. 2010) sources:							
SMM J22471	10.3 ± 3.1	38.2 ± 5.0	15.9 ± 5.0	9.1 ± 2.8	85 ± 10	$0.11\pm^{0.03}_{0.03}$	AOR:16175616
SMM J12	10.7 ± 0.2	46.1 ± 2.0	6.1 ± 0.6	6.7 ± 0.5	152 ± 38	$0.04\pm^{0.01}_{0.01}$	(Pope et al. 2008)
MIPS J14282	23.2 ± 3.6	94.7 ± 10.1	19.8 ± 2.5	11.1 ± 1.4	...	<0.12[a]	AOR:12513536
SWIRE L25	4.4 ± 0.3	12.6 ± 0.9	2.8 ± 0.6	3.2 ± 0.9	28 ± 2	$0.06\pm^{0.02}_{0.02}$	(Fiolet et al. 2010)
SWIRE L17	2.9 ± 0.3	14.4 ± 1.6	3.6 ± 0.6	2.8 ± 0.8	33 ± 6	$0.09\pm^{0.02}_{0.02}$	(Fiolet et al. 2010)

Notes. AOR refers to AORkey codes used to acquire spectra from CASSIS (Lebouteiller et al. 2011). References refer to publications of PAH spectra. MIR spectra for the sources with references are published spectra for which electronic copies of the data were acquired through private communication with publication authors.
[a] 7.7/11.2 μm PAH feature flux ratio makes Equation (4) poorly defined for MIPS J14282. Upper limit set by total of 6.2, through 11.2 μm PAH features.

[C II], as previously mentioned, arises in both neutral and ionized gas. Without other observations characterizing the ionized medium, we cannot be certain what fraction of the observed [C II] should be accounted for by the PDR models. Previous studies of many systems with [N II] and [C II] have shown the fraction of [C II] from PDRs generally ranges from ~40%–90% (Malhotra et al. 2001; Vasta et al. 2010). Although recent observations of extreme Lyman Alpha Emitters have revealed rare sources in which most of the [C II] arises in H II regions, Decarli et al. (2014) confirm that in SMGs [C II] is dominated by PDRs. In particular, in nearby starburst sources NGC 253 (Carral et al. 1994) and M82 (Lord et al. 1996; Colbert et al. 1999) combined H II and PDR modeling has shown ~70% of the [C II] emission comes from PDRs and we take these

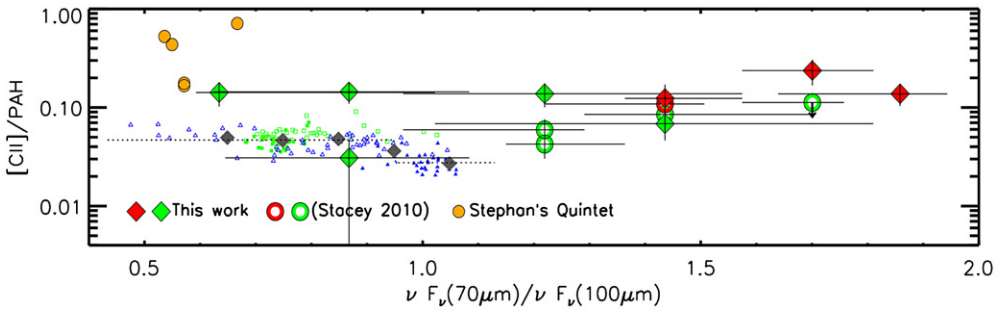

Figure 11. Figure adapted from Figure 8 of Croxall et al. (2012). [C II]/PAH vs. FIR color. [C II] is the observed line flux and PAH is the calculated total PAH flux based on Equation (4) with the qualifications noted in the text. Our sources (plotted as in previous figures) are plotted against sub-galactic star-forming regions in NGC 1097 (light blue triangles) and NGC 4559 (light green squares; see Croxall et al. 2012). We have also plotted regions from (Stacey et al. 2010b) and Stephan's Quintet as in previous figures. Our sample tends to lie between the [C II]/PAH ratios in Stephan's Quintet and those in local star-forming regions.

sources as representative analogs of our systems. This fraction is also very similar to the median contribution to [C II] from PDRs in the sample of Vasta et al. (2010). As a representative model, we therefore assume PDR-derived [C II] emission is equal to 70% of observed. Even if the actual amount of [C II] from PDRs in our systems is as small as 40% (the minimum in the sample of Vasta et al. 2010), this would only modestly effect our derived PDR conditions, raising the log(G_0) of our sample by an average of 22%. Our conclusions based on the modest strength of the FUV fields are, therefore, relatively robust to the uncertainty in [C II] attributed to PDRs.

In the analysis that follows, we compare PDR model grids of [C II], [O I], and IR continuum to our observations to create two-dimensional likelihood functions of the density and FUV irradiation strength that characterize each of our sources. We then integrate the likelihood function over one parameter at a time to create marginalized probability distributions for log(n) and log(G_0). We characterize these distributions using the most likely value with asymmetric error bars capturing 68.27% of the total probability distribution. In many cases, our observations support a double peaked two-dimensional likelihood function with one maxima at modest n and G_0 and one at high n and very low G_0. We favor the modest n, G_0 solution as the density is more representative of a mixed phase galaxy average, and, as we show in Section 5, a very low G_0 value is difficult to reconcile with the large luminosities of our systems. We have, therefore, imposed a prior to rule out solutions with log(G_0) $\leqslant 0.5$. Table 5 gives the PDR parameters required by the fitted models, and Figure 12 shows the PDR parameter space for our systems with constraints imposed by our observed line ratios.

MIPS 22530. Our [C II] and [O I] detections of this source are blueshifted relative to the optical redshift by ∼100 km s^{-1} and ∼200 km s^{-1}, respectively. MIPS 22530 is detected in all three MIPS bands and all three SPIRE bands, providing a well determined FIR SED. Its SED-derived luminosity is log($L_{\rm FIR}/L_\odot$) = 12.69 ± 0.04. The ratio of the two fine structure lines is similar to normal local galaxies, while the 60/100 μm flux density ratio is slightly warmer (see Figure 9). This source may also have a marginal AGN contribution (Sajina et al. 2008). This could be giving rise to a minor hot dust region, which contributes to the 60 μm emission without dominating the [O I] and [C II] lines. The fine structure lines in this source can be well described with a PDR model. Figure 12 shows the overlapping constraints placed on our PDR model from the [O I]/[C II] ratio and ([O I]+[C II])/IR. The multi-peaked probability distribution in our parameter space can be seen as the result of the two distinct intersections between the [O I]/[C II] contour and ([O I]+[C II])/IR. As discussed above, we favor the solution with modest density and G_0 rather than high density and low G_0. The PDR model constrains density, $n \sim 10^{3.75}$ cm^{-3} and UV flux $G_0 \sim 10^{2.25}$.

Table 5
PDR Model Parameters

Source	PDR Parameters		
	log(n cm^3)	log(G_0)	Size (kpc)
MIPS 22530	$3.75 \pm^{0.25}_{0.25}$	$2.25 \pm^{0.25}_{0.25}$	2.9–9.1
SWIRE 3-9	$3.5 \pm^{0.5}_{0.5}$	$2.5 \pm^{0.25}_{0.25}$	2.2–6.3
SWIRE 3-14	$3.5 \pm^{0.25}_{0.5}$	$2.75 \pm^{0.25}_{0.25}$	1.4–3.0
SWIRE 3-18	3–5	$2.0 \pm^{0.25}_{0.5}$	2.3–6.5
SMM J03	$3.25 \pm^{0.25}_{0.25}$	$2.25 \pm^{0.25}_{0.25}$	2.6–8.0
SWIRE 4-5	$4.25 \pm^{0.25}_{0.5}$	$1.25 \pm^{0.5}_{0.5}$	3.1–10.0
SWIRE 4-15	$4.25 \pm^{0.25}_{0.5}$	$2.25 \pm^{0.25}_{0.75}$	2.3–6.4
SDSS J12	$3.5 \pm^{0.25}_{0.25}$	$2.25 \pm^{0.25}_{0.25}$	2.6–7.6

Notes. The size scale represents the summed areal extent of star formation powered PDRs. It is a representative value only and its range is based on the most likely G_0 value under the separate assumptions of small and large mean free photon paths relative to cloud size as outlined in Section 5 (and does not account for the uncertainty on G_0 or the uncertainty in the fraction of [C II] from PDRs). Representative n and G_0 values give the best PDR solution assuming 70% of observed [C II] is due to PDRs. Error ranges are such that 68.27% of the power in the marginalized probability distribution of each parameter is contained within.

SWIRE 3-9 Both [C II] and [O I] are strongly detected in this source, although there appears to be a slight offset between the line centers, likely due to calibration error in the [C II] observation. Given the greater velocity resolution in the PACS [O I] spectrum, we adopt its indicated redshift of $z = 1.732 \pm 0.003$ with error bars encompassing our [C II] detection. The fine structure lines are significantly redward (∼2500 km s^{-1}) of the PAH-derived redshift, but agree within 1σ of the PAH redshift uncertainty. The PAH features are also well fit using our adopted redshift and the fitting quality is nearly equivalent to fits using the indicated PAH redshift. The fine structure lines and 60/100 μm flux density ratio are very similar to MIPS 22530. The fine structure lines are consistent with a star formation powered PDR source, and although the 60/100 μm flux density ratio is slightly warmer than our average source, the large uncertainty does not allow us to distinguish it from the normal local trend. Shown in Figure 12, [C II], [O I], and the FIR continuum constrain the PDR density, $n \sim 10^{3.5}$ and UV flux $G_0 \sim 10^{2.5}$.

SWIRE 3-14. Our [C II] line, detected at $z = 1.7795$, is consistent with PAH observations. Our PACS observations of

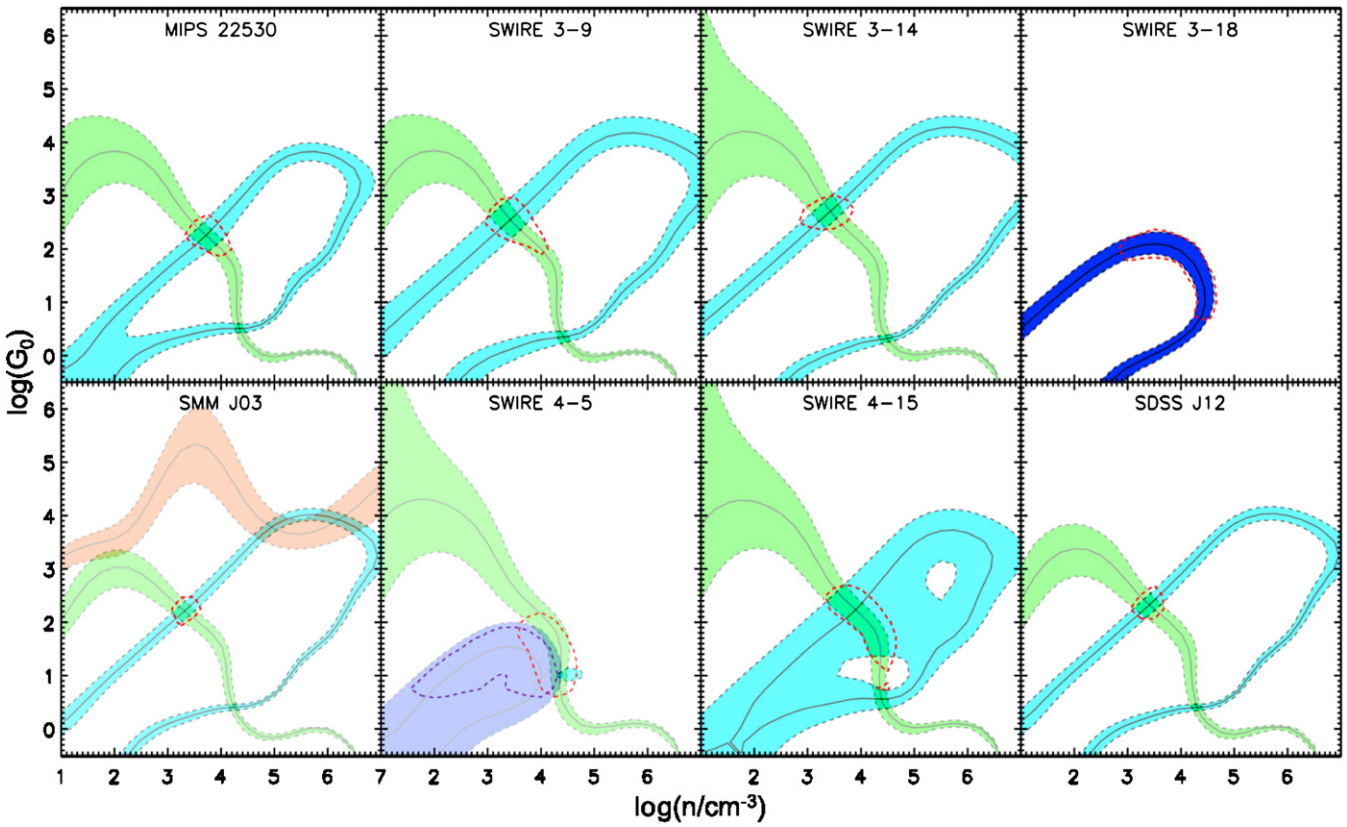

Figure 12. PDR diagnostic plots. Color shaded contours show constraints on n and G_0 based on the following ratios: green [O I]/[C II], cyan ([O I]+[C II])/IR, blue [C II]/IR, and orange [O I]/CO(3→2). Solid lines note ratio values and shaded areas represent $\pm 1\sigma$ regions. We attribute 70% of observed [C II] to the classic PDR model. Also overlaid as a dashed red line is the region containing 68.27% of the volume in the two-dimensional probability distribution of n and G_0. For source SWIRE 4-5, which has a tentative [O I] detection, we additionally show a purple dashed region indicating the 68.27% region that would result if we take the [O I] detection as an upper limit instead. Note that in this source the UV field is constrained to low intensities largely due to the [C II]/IR ratio, and the [O I] measurement mostly effects the density determination. We have assumed $G_0 > 10^{0.5}$ as a prior to ignore the low G_0 high density solution which, as discussed in the text, is unrealistic for galaxy averaged properties. In SWIRE 3-18, we lack a useful [O I]/[C II] ratio to constrain density so we have additionally assumed $n \sim 10^3 - 10^5$ cm^{-3}, consistent with other star-forming sources at high redshift (Stacey et al. 2010b).

this source detect the [O I] line at the [C II] velocity at $\sim 3\sigma$. The FIR SED of this source has a relatively low 60/100 μm flux density ratio. Although it has a high [C II]/FIR ratio, Figure 7 shows it is similar to local star-forming systems with equivalent FIR colors, suggesting this system is forming stars like local normal galaxies scaled up in size (or lensed.) As shown in Figure 12, [C II], [O I], and the FIR continuum constrain the PDR density, $n \sim 10^{3.5}$ and UV flux $G_0 \sim 10^{2.75}$.

SWIRE 3-18 is one of the strongest [C II] emitters with [C II]/FIR = 0.022 ± 0.004. We have compiled SPIRE photometry from HerMES to determine that it has a luminosity $\log(L_{\rm FIR}/L_\odot) = 12.13 \pm 0.13$ and a cool dust temperature with $F_\nu(60)/F_\nu(100) = 0.43\pm^{0.15}_{0.14}$, similar to SWIRE 4-5 and 4-15. This is consistent with previous claims that it is an SF-D source. Without an [O I] observation, we cannot fully disentangle density and G_0 degeneracies in the PDR model, but imposing an additional prior assumption that $n \sim 10^{3-5}$ cm^{-3} (a typical value for galaxies Stacey et al. 2010b) we find $G_0 \sim 10^{1.75}$ (Figure 12).

SMM J03 has a warm dust color, a high [C II]/FIR ratio, and an [O I]/[C II] ratio that falls below local sources with equivalent 60/100 μm flux density ratios. There are indications for marginal contribution from an AGN in this system (Swinbank et al. 2004; Takata et al. 2006). As we suggested for MIPS 22530, the [O I] and [C II] emission may be dominated by star formation spread throughout the disk, while an AGN fueled hot dust region may contribute to the 60 μm flux. In addition, CO 3→2 has been detected in this source, $F_{\rm CO(3\to2)} = (6.4 \pm 1.9)\times10^{-21}$ W m^{-2} (S. Hailey-Dunsheath 2013, private communication). Figure 12 shows our PDR model for the fine structure lines ([C II], [O I]), FIR continuum, and CO emission. Our PACS photometry along with SCUBA data (Kovács et al. 2006) provide a well-constrained SED with $\log(L_{\rm FIR}/L_\odot) = 12.58 \pm 0.03$. Our [C II], [O I], and infrared continuum observations are consistent with a standard PDR model. The CO 3→2 flux, however, appears too low for a standard PDR given our observed fine structure lines. It would need to be a factor of 10 higher for the [O I]/CO 3→2 ratio (orange contour, Figure 12) to be in agreement with the other line ratios. This is probably evidence for low metallicity, as suppressed CO is a common feature in low metallicity systems (Stacey et al. 1991; Poglitsch et al. 1995; Smith & Madden 1997). Since we do not have other constraints on the metallicity of this system, we ignore the CO flux in fitting our PDR model. The [O I], [C II], and infrared continuum, are consistent with star formation powered PDRs with a modest UV intensity $G_0 \sim 10^{2.25}$, and density $n \sim 10^{3.25}$ cm^{-3}.

SWIRE 4-5. The [C II] line is detected at $z = 1.756$, consistent with the previous PAH determined redshift. The SED fit to FIR photometry reveals $\log(L_{\rm FIR}/L_\odot) = 11.73 \pm 0.19$ and $F_\nu(60)/F_\nu(100) = 0.30\pm^{0.24}_{0.01}$, making it the coolest dust temperature source in our sample. Furthermore, the resulting [C II]/FIR ratio, 0.042 ± 0.01, makes this one of the most exceptional [C II] emitters known. The [O I] spectrum shows a marginal detection. The line is consistent with the [C II] velocity and a normal local

[C II]/[O I] ratio; however, the spectrum is taken from an off center PACS pixel corresponding to 9.3 arc seconds off the nominal position. We present it here as a tentative detection.

It is reasonable to conclude that the [C II] and [O I] are coming from the same region in this source, but their particularly high fluxes relative to the FIR make it difficult to rectify with a classic PDR model in which UV photons dominate the gas heating. In particular, the maximum ([C II]+[O I]) to infrared continuum ratio predicted by the PDR models is only just able to capture the lower 1σ bound of our observations. In Table 5 and Figure 12, we show that this solution implies especially low FUV fields $G_0 \sim 10^{1.25}$. Since the [O I] detection is only tentative, we also show the [C II] to infrared continuum ratio in Figure 12 and note that if we treat the [O I] observation as an upper limit, PDR models still require an extremely low UV field ($G_0 \sim 10^{1.75}$).

Although PDRs are capable of recreating the observed line emission, they require very low intensity UV fields to dominate over the galaxy, and in Figures 6 and 9, SWIRE 4-5 is an outlier from trends seen in the local universe regardless of its uncertain [O I] emission or assumptions over PDR models. We discuss the implications of these results below.

SWIRE 4-15. Our [C II] detection at $z = 1.8540$ is well within the PAH determined redshift range. FIR photometry shows an SED dominated by a modestly cool dust component (with large uncertainty on the 60/100 μm flux ratio) peaking at $\sim$100 μm, suggesting low FUV intensity extended star formation. We find $\log(L_{\rm FIR}/L_\odot) = 12.36 \pm 0.15$ and $F_\nu(60)/F_\nu(100) = 0.69\pm^{0.29}_{0.19}$. We have a broad line detection in [O I], ($F_{[O\,I]} = 4.4 \pm 1.1\times10^{-18}$ W m^{-2}), yielding a [C II]/[O I] ratio similar to normal galaxies. Our PDR model requires modest FUV fields densities to explain the emission ($G_0 \sim 10^{2.25}$, $n \sim 10^{4.25}$).

SDSS J12. This source was observed and detected in [O I] by Sangeeta Malhotra and well constrained in the FIR continuum by PACS and SPIRE photometry measurements from the *SEDs and energetics of lensed UV-bright high redshift galaxies* project. We add to the discussion our [C II] observation, and the PAHfit MIR spectrum. The FIR photometry yields an apparent $\log(L_{\rm FIR}/L_\odot) = 12.54 \pm 0.03$. Accounting for the system magnification ($\sim$27), the intrinsic luminosity suggests that SDSS J12 is a relatively modest star-forming source in terms of overall luminosity. SDSS J12 has the warmest FIR color in our sample, $F_\nu(60)/F_\nu(100) = 1.23\pm^{0.08}_{0.20}$. This may be due to exceptionally strong recent or ongoing star formation, which would cause increased abundance of hot dust along with ionized gas reserves (Hainline et al. 2009a). Alternatively, this source may in fact have an AGN that contributes significantly to the 60 μm emission. In Figure 12 we show that a PDR model with $\log(n) \sim 3.5$ and $\log(G_0) \sim 2.25$ can explain the [C II] and [O I] emission along with the continuum.

5. DISCUSSION

Our source sample is dominated by galaxies that lie along the galaxy's main sequence, powered by star formation. This is a reflection of our selection bias toward star-forming sources due to our selection criteria requiring PAH emission. We have confirmed our previous result (Stacey et al. 2010b) that the [C II] deficit is not a ubiquitous phenomenon in star formation powered ULIRGs at redshifts 1–2.

If we interpret our observations within the PDR paradigm, as is the common practice for [C II] and [O I], then the relative strengths of [C II], [O I], and the infrared continuum characterize the density of the PDR media and the intensity of the local FUV field. In general, the densities that characterize our sources are of the order of, or slightly greater than, the [C II] critical density. This suggests that the [C II] line is cooling the PDR gas at nearly maximum efficiency, consistent with the high [C II]/FIR ratios we observe.

The FUV intensity we derive from the PDR models can be related to the integrated source luminosity. Essentially, all of the FUV that impinges on neutral gas clouds is absorbed by dust and reradiated in the FIR continuum. Therefore, the observed infrared intensity measures the average FUV field intensity within our telescope beam. The PDR-derived FUV field intensity, (G_0), and our beam-averaged field intensity are thus related by the source beam filling factor.

We can consider this beam filling factor in the form of a back of the envelope calculation. Wolfire et al. (1990) found that a cloud of size D, and luminosity, $L_{\rm IR}$, should have an average FUV field given by $G_0 \propto \lambda L_{\rm IR}/D^3$ where λ, the mean-free path of a photon, is much smaller than the cloud extent, D; or $G_0 \propto L_{\rm IR}/D^2$ if $\lambda \gtrsim D$. Detailed models of the physical conditions of the molecular interstellar medium (ISM) in the star-forming regions of the nearby starburst galaxy M82 are remarkably similar to the average values we find for our sources, namely, $n \sim 10^4$ cm^{-3} and $G \sim 10^3$ (Lord et al. 1996), so that we use it as a template by which we scale our redshift 1–2 sample. Note that strictly this comparison also requires that the relative distribution of star formation (extended versus nuclear) be similar between M82 and our sources. Without resolved observations of our sample it is unclear whether this is the case, so we proceed with the expectation that our findings will be indicative of the order of magnitude only.

For M82, if we take $D \sim 300$ pc (Joy et al. 1987) and $L_{\rm FIR} \sim 2.8 \times 10^{10} L_\odot$, we find that $(D/{\rm pc})^3 \sim 0.96\,(L_{\rm FIR}/L_\odot)/G_0$ or $(D/{\rm pc})^2 \sim 3.2{\rm e}{-3}\,(L_{\rm FIR}/L_\odot)/G_0$. As noted in Table 5, we find the spatial extent of star formation in all of our sources is $\gtrsim$1 kpc, implying that star formation is occurring over a large fraction of the galactic disk. Note that a lower FUV field intensity, $G_0 \sim 10^{0.25}$, which often appears as a secondary solution in our PDR models comparing [C II] and [O I] (see Figure 12), would imply spatial scales that are of an order of magnitude larger, which is not reasonable, so we take the higher FUV field solution. Similar analysis by Díaz-Santos et al. (2014) of a sample of local LIRGs shows that there is indeed a strong correlation between the FUV intensity and emitting region size, but suggests that, on a galaxy-wide scale on average, $G_0 \propto L_{\rm IR}/D^\alpha$ where $\alpha < 2$. This implies that, if anything, our estimates of the emitting size regions is an underestimate.

Our finding of kiloparsec-scale star formation is consistent with recent observations of spatially resolved CO in high redshift sources (Tacconi et al. 2010; Daddi et al. 2010; Ivison et al. 2011; Riechers et al. 2011). As Tacconi et al. (2010) point out, the large spatial distribution of molecular gas does not necessarily imply a single coherent disk of star formation, but instead is very likely the observation of widely distributed clumps that are not individually resolved, but are all likely undergoing star formation obeying a Schmidt–Kennicutt law.

As shown in Table 5, the combined [C II], [O I], and infrared continuum observations can only be fit within the PDR paradigm if the source size is, in all cases at least a kiloparsec, and, in many, potentially much larger. This is in sharp contrast with local ULIRGs, which have intense and concentrated collision-induced bursts of star formation occurring on sub-kiloparsec

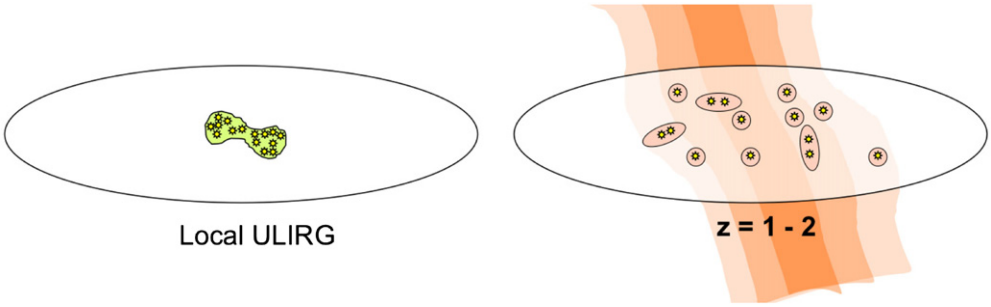

Figure 13. Schematic representation of star formation in local ULIRGs (left) vs. star formation powered ULIRGs at $z = 1$–2 (right.) Local ULIRGs may show one or more compact regions of intense star formation activity with strong UV fields and high dust temperatures, often powered by recent galaxy merging. At redshifts 1–2 the modest UV fields discussed here (as well as the spatially extended molecular gas observed by Tacconi et al. 2010; Daddi et al. 2010; Ivison et al. 2011; Riechers et al. 2011) indicate star formation spread out over a significant fraction of the galaxy's disk. We suggest that intergalactic gas accretion from the cosmic web (indicated by shaded region) fuels such widespread star formation.

scales. Figure 13 presents a cartoon schematic of these different modes of star formation.

The large spatial scales of star formation are best understood as the expected star formation that results from large and abundant molecular reserves under a Schmidt–Kennicutt law. The large molecular gas aggregation likely results from gas accretion from the cosmic web, and not coalescence from major mergers, which models show produce very intense, but spatially concentrated, star formation resulting in low [C II]/FIR ratios as seen in local ULIRGs. Under this interpretation, we suggest that, at least in our class of SF-D galaxies detected in PAH emission, much of the star formation in the epoch of peak star formation resulted from gas accretion from the cosmic web, and not solely merger activity as was once assumed.

In addition to [C II] and [O I] 63 μm observations, we have also compiled IRS spectra, which we have made use of here to consider PAH emission. In our sample, the PAH features are strong but, as we show in Figure 11, the [C II] to PAH ratios in many of our sources exceed those of local star formation regions.

This accumulated wealth of data has allowed for an unprecedented look at the nature of these galaxies, and in particular their dominant power sources for the far infrared cooling lines. The standard approach, using classic PDRs, can adequately produce the line and continuum emission we see. This does not fully explain why we would see such extensive low intensity UV PDRs in the case of SWIRE 4-5 (and SWIRE 3-18 to a lesser extent,) to produce a [C II]/FIR ratio that exceeds observations in the local universe. Indeed, the fine structure line emission relative to the infrared continuum in SWIRE 4-5 is brushing up against the limits of what classic PDRs are capable of producing. It would require clumps of uniformly low FUV powered PDRs distributed throughout the galaxy to produce such a high [C II]/FIR ratio.

In addition to the difficulty in modeling the fine structure line emission in these systems with PDRs, many of our sources (including SWIRE 4-5) have high [C II]/PAH ratios compared to nearby star-forming sub-galactic regions. This feature is particularly reminiscent of the work by Guillard et al. (2012) and Appleton et al. (2013) on Stephan's Quintet, a nearby interacting compact group of galaxies. Their work shows enhanced CO and [C II] emission in filamentary structures between the main sources in the group. They have shown that this is a direct result of shock heated gas. In these shock powered regions, Appleton et al. (2013) finds [C II]/FIR and [C II]/PAH ratios a factor of a few higher than we see (as shown in Figures 6 and 11), as well as cool FIR dust temperatures, similar to SWIRE 4-5 (Figures 4 and 7).

We have already seen cases where microturbulence contributes significantly to the overall heating budget of various lines on a galaxy-wide scale. In earlier work on NGC 253 and NGC 891, we found that microturbulence was needed in addition to classic PDRs to explain neutral and molecular gas emission (Hailey-Dunsheath et al. 2008; Stacey et al. 2010a; Nikola et al. 2011). Implicating microturbulence to explain [C II] emission requires a source of radiation to ionize the carbon. Models by Lesaffre et al. (2013; and invoked in Stephan's Quintet by Appleton et al. 2013) showed that diffuse gas undergoing low velocity turbulent shocks that heat the gas can cool by emission in the [C II] line if C+ is formed within the cloud by modest FUV radiation fields.

Although the resolved regions of Stephan's Quintet and our sources represent very different systems (shocked filamentary structures embedded in the IGM between interacting systems versus unresolved (U)LIRGs,) given the displacement of SWIRE 4-5 from local galaxy trends, and the empirical similarity between it and shock powered regions of Stephan's Quintet, it may be that SWIRE 4-5 represents a hybrid systems involving significant contributions from both classic PDRs and shock powered regions. Shock heating may in fact be a common contributor to [C II] emission especially in the early universe as IGM gas accretion becomes more ubiquitous.

However, this turbulent heating does not necessarily imply violent galaxy mergers. Indeed, low velocity shocks ($\sim$8 km s^{-1}) can efficiently heat gas and might contribute significantly to the observed [C II] line. Such low velocity shocks might be the result of galaxy interaction, as in the case of Stephan's Quintet, or might easily result from star formation feedback processes such as stellar outflow and supernovae, or impacting clumps and gas streams accreting from the intergalactic medium. With our spatially unresolved observations it is impossible to distinguish between these possibilities. To characterize the shock properties and the relative contributions from shocked diffuse gas and PDRs would either require spatially resolved observations or more diagnostic emission lines. MIR H_2 lines are particularly useful shocked gas diagnostics; unfortunately, their typical luminosities are one or two orders of magnitude weaker than PAH features, putting them below the sensitivity of our MIR spectra (Figure 10). Upper limits on the H_2 S(3) 0-0 line are noted in the Appendix (Table 7), but are unfortunately too high to constrain shock or PDR models. Although in SWIRE 4-5 (and to a lesser extent SWIRE 3-18,) the very

strong [C II] emission with respect to FIR and PAHs is a good indication that additional sources of heating are contributing to the [C II] emission, we cannot definitively say this is the case without further infrared and submillimeter observation. If similar sources are found to be common in the early universe, characterizing their emission mechanisms will be paramount to understanding galaxy evolution.

6. CONCLUSIONS

We have detected eight new $z = 1$–2 sources in the [C II] 157.7 μm line. Seven of them were also observed in the [O I] 63 μm line (six in our *Herschel* program and the seventh by Sangeeta Malhotra.) Far infrared photometry, made available through ours and other *Herschel* programs, has allowed us to establish SEDs providing reliable FIR luminosities and estimates of the FIR dust temperature.

Our sample selection required that sources be detected in PAH emission, biasing the sample toward sources with FIR luminosities dominated by star formation rather than AGNs. In general, we have found that the relative [C II] and [O I] emission is comparable to local star-forming systems and can largely be explained with classic PDR models. There is, however, very strong [C II] relative to both FIR continuum and PAH emission. Six of our eight sources exhibit both [C II]/FIR $> 10^{-2}$ and [C II]/PAH $_{\rm tot} > 0.1$. In most of our sources, their [C II]/FIR ratio is a factor of a few greater than found for local sources with comparable 60/100 μm flux density ratios.

We have used [C II]/FIR to determine G_0 based on a PDR paradigm, and with $L_{\rm FIR}$ we determine the PDR filling factor in our beam. Based on this model, the extent of our star-forming regions is very large, unlike local ULIRGs. This supports the scenario in which extended, moderate intensity, star formation pervades their disks, likely stimulated by large molecular gas reservoirs accreted from the cosmic web. Although drawing conclusions about the general $z = 1$–2 galaxy population based on our sample is beyond the scope of this paper, the results from our sample are consistent with the idea that much of the star formation at $z \sim 1$–2 is not driven by major mergers, but instead by cold flow accretion. Although there are several examples of major mergers in the early universe, our sample suggests cold flow accretion fueled galaxy star formation abounds as well. Our [O I] and PAH detections further confirm this interpretation of [C II].

While the [C II] and [O I] likely arise from classic PDRs, we must qualify the standard PDR paradigm with the caveat that the exceptionally strong [C II] emission from SWIRE 4-5 may be powered by other heating mechanisms as well. The high [C II]/FIR ratio is significantly larger than what is seen locally and even approaches the limit of what PDRs can provide. It is cool FIR dust temperature suggests that any additional mechanisms that may be heating the gas must not be producing significant amounts of hot dust. This is consistent with directly heating the gas via low velocity shocks in a diffuse gas component as modeled by Lesaffre et al. (2013) and invoked by Appleton et al. (2013) to explain high [C II] ratios in regions of Stephan's Quintet.

The [C II] line remains a useful probe in the $z > 1$ universe. It was once assumed that large-scale mergers dominated the star formation in this epoch that would lead to compact and intense star formation regions with relatively weak [C II] emission like local ULIRG galaxies. The discovery of very extended [C II] emission is a key element of the new paradigm that in many systems, cold accretion from the cosmic web fuels very high gas surface densities leading to enhanced, wide-scale star formation following a Schmidt–Kennicutt law typical of normal galaxies.

With the observational avenues that have opened in the last few years, we are now able to acquire more diversity of data and work with better refined models than ever before. This presents us with the welcome challenge of transitioning from studying broad brush characterization of star formation, in general, to examining individual sources. Going forward, the [C II] line, [O I], PAHs, and other multiwavelength data will allow us an exceptional look at the dynamics of individual galaxies, building on the picture presented here by further constraining the merger fraction of star-forming galaxies throughout cosmological time.

We thank the anonymous referee for insightful comments on previous drafts of this paper. ZEUS observations were supported by NSF grants AST-0705256, AST-0722220, and AST-1109476. We also thank the staff of the CSO for their support of ZEUS operations. This research has made use of data from HerMES project (http://hermes.sussex.ac.uk/). HerMES is a Herschel Key Programme utilizing Guaranteed Time from the SPIRE instrument team, ESAC scientists and a mission scientist. HerMES is described in (Oliver et al. 2012). The HerMES data was accessed through the HeDaM database (http://hedam.oamp.fr) operated by CeSAM and hosted by the Laboratoire d'Astrophysique de Marseille. The National Radio Astronomy Observatory is a facility of the National Science Foundation operated under cooperative agreement by Associated Universities, Inc.

APPENDIX

The general properties of galaxies in our sample, which we discuss in the text, are captured in the previous tables included in the manuscript. It was often useful, however, to use several related diagnostics to make comparisons to other samples from the literature (e.g., in addition to the 60/100 μm flux ratio, we made use of the 70/100 μm flux ratio). For brevity of the text, we include those data here, along with the detailed photometric data used in our SED fits.

Table 6
Photometry Used in SED Fitting

SWIRE 4-5	SWIRE 4-15	SWIRE 3-14	SWIRE 3-18	SWIRE 3-9	MIPS 22530	SDSS J12	SMM J03
MIPS 24	MIPS 24	MIPS 24	MIPS 24	MIPS 24	MIPS 24		MIPS 24
0.550 ± 0.015 [1]	0.419 ± 0.018 [1]	0.874 ± 0.016 [2]	0.761 ± 0.076 [2]	1.0 ± 0.1 [2]	1.23 ± 0.06 [3]		0.23 ± 0.02 [4]
							0.47 ± 0.05 [5]
					MIPS 70	PACS 70	PACS 70
					3.4 ± 1.9 [6]	9.7 ± 3.3 [7]	21.3 ± 4.4 [8]
						PACS 100	PACS 100
						16.5 ± 1.5 [7]	48.6 ± 3.5 [8]
					MIPS 160	PACS 160	PACS 160
					38.0 ± 9.0 [9]	39 ± 21 [7]	64.8 ± 6.5 [8]
SPIRE 250	SPIRE 250	SPIRE 250	SPIRE 250	SPIRE 250	SPIRE 250	SPIRE 250	
15.5 ± 6.3 [10]	28.1 ± 6.3 [10]	28.2 ± 7.4 [10]	25.9 ± 7.4 [10]	42.9 ± 7.4 [10]	61.4 ± 7.1 [10]	30.8 ± 2.4 [7]	
SPIRE 350	SPIRE 350	SPIRE 350	SPIRE 350	SPIRE 350	SPIRE 350	SPIRE 350	SHARC2 350
20 ± 10. [10]	28 ± 10. [10]	43.7 ± 5.4 [10]	42.0 ± 6.6 [10]	40.2 ± 6.6 [10]	52.8 ± 6.1 [10]	15.5 ± 4.6 [7]	42.2 ± 9.8 [11]
SPIRE 500	SPIRE 500	SPIRE 500	SPIRE 500	SPIRE 500	SPIRE 500	SPIRE 500	SCUBA 450
11.6 ± 5.0 [10]	17.4 ± 4.9 [10]	29.2 ± 7.1 [10]	28.1 ± 6.9 [10]	21.9 ± 6.9 [10]	26.3 ± 6.1 [10]	14.9 ± 8.4 [7]	<63 [12]
MAMBO 1200	MAMBO 1200				MAMBO 1200		SCUBA 850
2.75 ± 0.76 [1]	2.36 ± 0.62 [1]				2.11 ± 0.56 [9]		4.4 ± 1.3 [12]

Notes. Each entry gives instrument and wave band on the first line, followed by measurement and reference code on the second line. SPIRE 250, 350, and 500 μm uncertainties are set to 30% to account for potential confusion noise. In fitting the 24 μm photometry, we used 10 times the uncertainty quoted here to compensate for the inflexible treatment of PAH fluxes in the model grid. These photometry are not color corrected. In all cases, color correcting the PACS and SPIRE photometry resulted in changes less than 10%. References: [1] (Fiolet et al. 2009), [2] (Farrah et al. 2008), [3] (Fadda et al. 2006), [4] (Efstathiou & Siebenmorgen 2009), [5] (Hainline et al. 2009b), [6] (Sajina et al. 2007), [7] (Data from *Herschel* program *SEDs and energetics of lensed UV-bright high redshift galaxies* - flux extracted using standard HIPE methods), [8] (this work), [9] (Sajina et al. 2008), [10] (HerMES source catalog), [11] (Kovács et al. 2006), [12] (Webb et al. 2003).

Table 7
Fine Structure Lines, SED Properties, and $H_2S(3)$

Source	$\log(L/L_\odot)$ (μm range)				$\frac{F_\nu(60)}{F_\nu(100)}$	$\frac{F_\nu(70)}{F_\nu(100)}$	Line flux (10^{-18} W m^{-2})			$\frac{F_{[O\,I]}}{F_{[C\,II]}}$	$\frac{L_{[C\,II]}}{L_{[FIR]}}$	$\frac{L_{[O\,I]}}{L_{[FIR]}}$
	42.5–122.5	40–500	30–1000	8–1000			[C II]	[O I]	$H_2S(3)$[a]			
MIPS 22530	12.69 ± 0.04	12.79 ± 0.04	12.87 ± 0.04	12.96 ± 0.04	$0.87 \pm^{0.12}_{0.06}$	$1.01 \pm^{0.10}_{0.05}$	9.3 ± 2.1	5.4 ± 1.1	<3.7	0.59 ± 0.18	(1.4 ± 0.3)E -2	(8.0 ± 1.8)E -3
SWIRE 3-9	12.59 ± 0.15	12.67 ± 0.13	12.75 ± 0.15	12.83 ± 0.16	$0.87 \pm^{0.32}_{0.32}$	$1.01 \pm^{0.26}_{0.29}$	6.4 ± 1.4	3.8 ± 0.8	<1.9	0.59 ± 0.18	(8.9 ± 3.7)E -3	(5.2 ± 2.1)E -3
SWIRE 3-14	12.21 ± 0.13	12.45 ± 0.08	12.47 ± 0.08	12.55 ± 0.08	$0.43 \pm^{0.15}_{0.13}$	$0.61 \pm^{0.15}_{0.16}$	2.3 ± 0.4	1.6 ± 0.5	<3.9	0.69 ± 0.24	(8.3 ± 2.9)E -3	(5.7 ± 2.4)E -3
SWIRE 3-18	12.13 ± 0.13	12.39 ± 0.08	12.42 ± 0.09	12.49 ± 0.09	$0.43 \pm^{0.15}_{0.14}$	$0.61 \pm^{0.15}_{0.17}$	5.5 ± 1.0	···	<2.4	···	(2.3 ± 0.8)E -2	···
SMM J03	12.58 ± 0.03	12.66 ± 0.03	12.75 ± 0.03	12.85 ± 0.03	$1.09 \pm^{0.10}_{0.11}$	$1.19 \pm^{0.08}_{0.09}$	16.9 ± 3.5	6.0 ± 0.9	<5.0	0.353 ± 0.089	(1.5 ± 0.3)E -2	(5.1 ± 0.8)E -3
SWIRE 4-5	11.73 ± 0.19	12.01 ± 0.14	12.03 ± 0.15	12.11 ± 0.15	$0.30 \pm^{0.24}_{0.01}$	$0.44 \pm^{0.27}_{0.03}$	4.5 ± 1.1	3.2 ± 1.0	<0.6	0.72 ± 0.28	(4.7 ± 2.4)E -2	(3.3 ± 1.8)E -2
SWIRE 4-15	12.36 ± 0.15	12.48 ± 0.12	12.53 ± 0.14	12.62 ± 0.15	$0.69 \pm^{0.29}_{0.19}$	$0.85 \pm^{0.25}_{0.18}$	5.0 ± 1.3	3.6 ± 0.9	<0.6	0.71 ± 0.26	(1.4 ± 0.6)E -2	(9.9 ± 4.3)E -3
SDSS J12	12.54 ± 0.03	12.62 ± 0.03	12.72 ± 0.03	12.82 ± 0.03	$1.23 \pm^{0.08}_{0.20}$	$1.30 \pm^{0.06}_{0.15}$	5.6 ± 1.4	2.5 ± 0.5	<0.3	0.45 ± 0.14	(1.3 ± 0.3)E -2	(5.6 ± 1.1)E -3

Note. [a] H_2 S(3) measurements are 3σ upper limits based on the noise in MIR IRS spectra at 9.615 μm.

REFERENCES

Appleton, P. N., Guillard, P., Boulanger, F., et al. 2013, ApJ, 777, 66
Armus, L., Mazzarella, J. M., Evans, A. S., et al. 2009, PASP, 121, 559
Bell, E. F., McIntosh, D. H., Katz, N., & Weinberg, M. D. 2003, ApJS, 149, 289
Brandl, B. R., Bernard-Salas, J., Spoon, H. W. W., et al. 2006, ApJ, 653, 1129
Brauher, J. R., Dale, D. A., & Helou, G. 2008, ApJS, 178, 280
Carral, P., Hollenbach, D. J., Lord, S. D., et al. 1994, ApJ, 423, 223
Chabrier, G. 2003, ApJL, 586, L133
Chapman, S. C., Blain, A. W., Smail, I., & Ivison, R. J. 2005, ApJ, 622, 772
Colbert, J. W., Malkan, M. A., Clegg, P. E., et al. 1999, ApJ, 511, 721
Coppin, K. E. K., Danielson, A. L. R., Geach, J. E., et al. 2012, MNRAS, 427, 520
Crawford, M. K., Genzel, R., Townes, C. H., & Watson, D. M. 1985, ApJ, 291, 755
Croxall, K. V., Smith, J. D., Wolfire, M. G., et al. 2012, ApJ, 747, 81
Daddi, E., Alexander, D. M., Dickinson, M., et al. 2007, ApJ, 670, 173
Daddi, E., Bournaud, F., Walter, F., et al. 2010, ApJ, 713, 686
Dale, D. A., & Helou, G. 2002, ApJ, 576, 159
Dale, D. A., Helou, G., Brauher, J. R., et al. 2004, ApJ, 604, 565
Dalgarno, A., & McCray, R. A. 1972, ARA&A, 10, 375
De Breuck, C., Maiolino, R., Caselli, P., et al. 2011, A&A, 530, L8
de Jong, R. S. 1996, A&A, 313, 377
Decarli, R., Walter, F., Carilli, C., et al. 2014, ApJL, 782, L17
Desai, V., Soifer, B. T., Dey, A., et al. 2009, ApJ, 700, 1190
Díaz-Santos, T., Armus, L., Charmandaris, V., et al. 2014, ApJL, 788, L17
Díaz-Santos, T., Armus, L., Charmandaris, V., et al. 2013, ApJ, 774, 68
Efstathiou, A., & Siebenmorgen, R. 2009, A&A, 502, 541
Elbaz, D., Dickinson, M., Hwang, H. S., et al. 2011, A&A, 533, A119
Fadda, D., Marleau, F. R., Storrie-Lombardi, L. J., et al. 2006, AJ, 131, 2859
Fadely, R., Allam, S. S., Baker, A. J., et al. 2010, ApJ, 723, 729
Farrah, D., Lebouteiller, V., Spoon, H. W. W., et al. 2013, ApJ, 776, 38
Farrah, D., Lonsdale, C. J., Borys, C., et al. 2006, ApJL, 641, L17
Farrah, D., Lonsdale, C. J., Weedman, D. W., et al. 2008, ApJ, 677, 957
Ferkinhoff, C., Brisbin, D., Parshley, S., et al. 2014, ApJ, 780, 142
Fiolet, N., Omont, A., Lagache, G., et al. 2010, A&A, 524, A33
Fiolet, N., Omont, A., Polletta, M., et al. 2009, A&A, 508, 117
Gallerani, S., Neri, R., Maiolino, R., et al. 2012, A&A, 543, A114
Graciá-Carpio, J., Sturm, E., Hailey-Dunsheath, S., et al. 2011, ApJL, 728, L7
Griffin, M. J., Abergel, A., Abreu, A., et al. 2010, A&A, 518, L3
Guillard, P., Boulanger, F., Pineau des Forêts, G., et al. 2012, ApJ, 749, 158
Hailey-Dunsheath, S. 2009, PhD thesis, Cornell Univ.
Hailey-Dunsheath, S., Nikola, T., Stacey, G. J., et al. 2008, ApJL, 689, L109
Hainline, K. N., Shapley, A. E., Kornei, K. A., et al. 2009a, ApJ, 701, 52
Hainline, L. J., Blain, A. W., Smail, I., et al. 2009b, ApJ, 699, 1610
Hildebrand, R. H., Loewenstein, R. F., Harper, D. A., et al. 1985, Icar, 64, 64
Hodge, J. A., Carilli, C. L., Walter, F., et al. 2012, ApJ, 760, 11

Houck, J. R., Roellig, T. L., Van Cleve, J., et al. 2004, Proc. SPIE, 5487, 62
Huang, J.-S., Faber, S. M., Daddi, E., et al. 2009, ApJ, 700, 183
Ivison, R. J., Papadopoulos, P. P., Smail, I., et al. 2011, MNRAS, 412, 1913
Ivison, R. J., Swinbank, A. M., Swinyard, B., et al. 2010, A&A, 518, L35
Joy, M., Lester, D. F., & Harvey, P. M. 1987, ApJ, 319, 314
Kaufman, M. J., Wolfire, M. G., & Hollenbach, D. J. 2006, ApJ, 644, 283
Kennicutt, R. C., Jr. 1998, ApJ, 498, 541
Kovács, A., Chapman, S. C., Dowell, C. D., et al. 2006, ApJ, 650, 592
Lebouteiller, V., Barry, D. J., Spoon, H. W. W., et al. 2011, ApJS, 196, 8
Lesaffre, P., Pineau des Forêts, G., Godard, B., et al. 2013, A&A, 550, A106
Lin, H., Buckley-Geer, E., Allam, S. S., et al. 2009, ApJ, 699, 1242
Lonsdale, C. J., Polletta, M. d. C., Omont, A., et al. 2009, ApJ, 692, 422
Lonsdale, C. J., Smith, H. E., Rowan-Robinson, M., et al. 2003, PASP, 115, 897
Lord, S. D., Hollenbach, D. J., Haas, M. R., et al. 1996, ApJ, 465, 703
Luhman, M. L., Satyapal, S., Fischer, J., et al. 2003, ApJ, 594, 758
Magdis, G. E., Rigopoulou, D., Huang, J.-S., & Fazio, G. G. 2010, MNRAS, 401, 1521
Maiolino, R., Caselli, P., Nagao, T., et al. 2009, A&A, 500, L1
Maiolino, R., Cox, P., Caselli, P., et al. 2005, A&A, 440, L51
Malhotra, S., Kaufman, M. J., Hollenbach, D., et al. 2001, ApJ, 561, 766
Marsden, S. C., Waite, I. A., Carter, B. D., & Donati, J.-F. 2005, MNRAS, 359, 711
Menéndez-Delmestre, K., Blain, A. W., Smail, I., et al. 2009, ApJ, 699, 667
Mookerjea, B., Kramer, C., Buchbender, C., et al. 2011, A&A, 532, A152
Negishi, T., Onaka, T., Chan, K.-W., & Roellig, T. L. 2001, A&A, 375, 566
Nikola, T., Geis, N., Herrmann, F., et al. 2001, ApJ, 561, 203
Nikola, T., Stacey, G. J., Brisbin, D., et al. 2011, ApJ, 742, 88
Noeske, K. G., Faber, S. M., Weiner, B. J., et al. 2007, ApJL, 660, L47
Nordon, R., Lutz, D., Shao, L., et al. 2010, A&A, 518, L24
Oberst, T. E., Parshley, S. C., Stacey, G. J., et al. 2006, ApJL, 652, L125
Oliver, S. J., Bock, J., Altieri, B., et al. 2012, MNRAS, 424, 1614
Ott, S. 2010, in ASP Conf. Ser. 434, Astronomical Data Analysis Software and Systems XIX, ed. Y. Mizumoto, K.-I. Morita, & M. Ohishi (San Francisco, CA: ASP), 139
Pety, J., Beelen, A., Cox, P., et al. 2004, A&A, 428, L21
Pilbratt, G. L., Riedinger, J. R., Passvogel, T., et al. 2010, A&A, 518, L1
Poglitsch, A., Krabbe, A., Madden, S. C., et al. 1995, ApJ, 454, 293
Poglitsch, A., Waelkens, C., Geis, N., et al. 2010, A&A, 518, L2
Pope, A., Chary, R.-R., Alexander, D. M., et al. 2008, ApJ, 675, 1171
Pope, A., Scott, D., Dickinson, M., et al. 2006, MNRAS, 370, 1185
Pound, M. W., & Wolfire, M. G. 2008, in ASP Conf. Ser. 394, Astronomical Data Analysis Software and Systems XVII, ed. R. W. Argyle, P. S. Bunclark, & J. R. Lewis (San Francisco, CA: ASP), 654
Riechers, D. A., Bradford, C. M., Clements, D. L., et al. 2013, Natur, 496, 329
Riechers, D. A., Hodge, J., Walter, F., Carilli, C. L., & Bertoldi, F. 2011, ApJL, 739, L31
Rujopakarn, W., Rieke, G. H., Papovich, C. J., et al. 2012, ApJ, 755, 168
Sajina, A., Yan, L., Armus, L., et al. 2007, ApJ, 664, 713
Sajina, A., Yan, L., Lutz, D., et al. 2008, ApJ, 683, 659
Schmidt, M. 1959, ApJ, 129, 243
Serjeant, S. 2012, MNRAS, 424, 2429
Smith, B. J., & Madden, S. C. 1997, AJ, 114, 138
Smith, J. D. T., Draine, B. T., Dale, D. A., et al. 2007, ApJ, 656, 770
Stacey, G. J., Charmandaris, V., Boulanger, F., et al. 2010a, ApJ, 721, 59
Stacey, G. J., Geis, N., Genzel, R., et al. 1991, ApJ, 373, 423
Stacey, G. J., Hailey-Dunsheath, S., Ferkinhoff, C., et al. 2010b, ApJ, 724, 957
Stacey, G. J., Hailey-Dunsheath, S., Nikola, T., et al. 2007, in ASP Conf. Ser. 375, From Z-Machines to ALMA: (Sub)Millimeter Spectroscopy of Galaxies, ed. A. J. Baker, J. Glenn, A. I. Harris, J. G. Mangum, & M. S. Yun (San Francisco, CA: ASP), 52
Stacey, G. J., Smyers, S. D., Kurtz, N. T., & Harwit, M. 1983, ApJL, 268, L99
Stierwalt, S., Armus, L., Surace, J. A., et al. 2013, ApJS, 206, 1
Sturm, E., Verma, A., Graciá-Carpio, J., et al. 2010, A&A, 518, L36
Swinbank, A. M., Karim, A., Smail, I., et al. 2012, MNRAS, 427, 1066
Swinbank, A. M., Smail, I., Chapman, S. C., et al. 2004, ApJ, 617, 64
Symeonidis, M., Vaccari, M., Berta, S., et al. 2013, MNRAS, 431, 2317
Tacconi, L. J., Genzel, R., Neri, R., et al. 2010, Natur, 463, 781
Takata, T., Sekiguchi, K., Smail, I., et al. 2006, ApJ, 651, 713
Tielens, A. G. G. M., & Hollenbach, D. 1985, ApJ, 291, 722
Valtchanov, I., Virdee, J., Ivison, R. J., et al. 2011, MNRAS, 415, 3473
Vasta, M., Barlow, M. J., Viti, S., Yates, J. A., & Bell, T. A. 2010, MNRAS, 404, 1910
Venemans, B. P., McMahon, R. G., Walter, F., et al. 2012, ApJL, 751, L25
Wagg, J., Wiklind, T., Carilli, C. L., et al. 2012, ApJL, 752, L30
Wang, R., Wagg, J., Carilli, C. L., et al. 2013, ApJ, 773, 44
Webb, T. M., Eales, S. A., Lilly, S. J., et al. 2003, ApJ, 587, 41
Weingartner, J. C., & Draine, B. T. 2001, ApJS, 134, 263
Willott, C. J., Omont, A., & Bergeron, J. 2013, ApJ, 770, 13
Wolfire, M. G., Tielens, A. G. G. M., & Hollenbach, D. 1990, ApJ, 358, 116
Yan, L., Sajina, A., Fadda, D., et al. 2007, ApJ, 658, 778